

See discussions, stats, and author profiles for this publication at: <https://www.researchgate.net/publication/216591501>

15. Exploration of Electrostatic Field Force in Surface Enhanced Raman Scattering: An Experimental Investigation Aided by Density Functional Calculations

ARTICLE in THE JOURNAL OF PHYSICAL CHEMISTRY C · NOVEMBER 2008

Impact Factor: 4.77 · DOI: 10.1021/jp804028w

CITATIONS

26

READS

52

8 AUTHORS, INCLUDING:



Surojit Pande

Birla Institute of Technology and Science P...

45 PUBLICATIONS 1,635 CITATIONS

SEE PROFILE



Arun Kumar Sinha

Seoul National University

11 PUBLICATIONS 124 CITATIONS

SEE PROFILE



Tarasankar Pal

IIT Kharagpur

256 PUBLICATIONS 8,775 CITATIONS

SEE PROFILE



Joydeep Chowdhury

Jadavpur University

71 PUBLICATIONS 631 CITATIONS

SEE PROFILE

Article

**Exploration of Electrostatic Field Force in
Surface-Enhanced Raman Scattering: An Experimental
Investigation Aided by Density Functional Calculations**

Sougata Sarkar, Surojit Pande, Subhra Jana, Arun Kumar Sinha, Mukul
Pradhan, Mrinmoyee Basu, Joydeep Chowdhury, and Tarasankar Pal

J. Phys. Chem. C, **2008**, 112 (46), 17862-17876 • DOI: 10.1021/jp804028w • Publication Date (Web): 28 October 2008

Downloaded from <http://pubs.acs.org> on November 21, 2008

More About This Article

Additional resources and features associated with this article are available within the HTML version:

- Supporting Information
- Access to high resolution figures
- Links to articles and content related to this article
- Copyright permission to reproduce figures and/or text from this article

[View the Full Text HTML](#)



ACS Publications
High quality. High impact.

The Journal of Physical Chemistry C is published by the American Chemical Society, 1155 Sixteenth Street N.W., Washington, DC 20036

Exploration of Electrostatic Field Force in Surface-Enhanced Raman Scattering: An Experimental Investigation Aided by Density Functional Calculations

Sougata Sarkar,[†] Surojit Pande,[†] Subhra Jana,[†] Arun Kumar Sinha,[†] Mukul Pradhan,[†] Mrinmoyee Basu,[†] Joydeep Chowdhury,[‡] and Tarasankar Pal^{*,†}

Department of Chemistry, Indian Institute of Technology, Kharagpur 721302, India, and Department of Physics, Sammilani Mahavidyalaya, Baghajatin Station, E. M. Bypass, Kolkata 700 075, India

Received: May 7, 2008; Revised Manuscript Received: September 17, 2008

Surface chemical properties of metal nanoparticles must be tunable to create chemical specificity and are a key prerequisite for successful sensing and imaging platforms. To relate surface enhanced Raman scattering (SERS) to electrostatic field force, a simple colloidal chemistry approach has been deliberately exploited for syntheses of gold nanoparticles with negative and positive surface charges to study their interactions with charged analytes. We took up the challenge with sulfur-containing analytes because “Au–S” interaction is well-known. Thiocyanate ion, SCN^- , a well-known SERS analyte, has been proved to be chemically ligated/anchored on positively charged gold nanoparticles surface owing to favorable electrostatic attraction. The Au–S vibrational band at $\sim 240\text{ cm}^{-1}$ and blue-shifting of the $\text{C}\equiv\text{N}$ stretching frequency by $\sim 46\text{ cm}^{-1}$ in conjunction with its intensity enhancement by an order of $\sim 10^3$ in the SERS spectrum clearly illustrate a chemisorption phenomenon. In contrast, physisorption of the SCN^- ion becomes evident on negatively charged colloid. Again, methylene blue has been shown to remain engrossed on the negatively charged gold surfaces. However, the electrostatic field force could not be accounted for from fluorescence quenching while methylaminopyrene was introduced because of the distance-dependence effect. The feasibility of such coordinative/chemical attachment also has been examined theoretically by density functional theory (DFT). Moreover, employment of this DFT calculation has been performed on five different metal–molecule interaction models to fruitfully interpret the experimental SERS findings and also the orientation of the SERS analyte. The observed Raman signals have been assigned from the potential energy distributions in terms of internal coordinates of adsorbate from the output of DFT calculations. The results thus provide a benchmark illustration of the value of DFT for aiding interpretation of adsorbate vibrational spectra attainable by using SERS.

1. Introduction

Following initial observation by Fleischman et al. in 1974¹ and subsequent identification,² surface-enhanced Raman scattering (SERS) has revolutionized thought about the nature and orientation of adsorbed molecular species and the metal–adsorbate interaction mechanism at surfaces and interfaces.³ A typical Raman cross section of a molecule is about 10^6 and 10^{14} times smaller than the infrared and fluorescence cross sections, respectively.⁴ For in situ Raman studies of most adsorbates, the intensities of the Raman signals were so low that they were at (or under) the detection limits of the instruments. Therefore, one must use SERS to boost the detection sensitivity enormously. The recent advent of SERS has provided the detailed vibrational information for species present at trace concentrations down to the single molecule level.⁵ Recent findings have made SERS a versatile technique having a diverse field of applications not only in analytical sciences but also in biomedicine, environmental monitoring, artwork conservation, corrosion, lubrication, explosives, nanotechnology, and heterogeneous catalysis.⁶ Despite all of these advantages, SERS has limitations in analytical figures of merit, such as reproducibility and dynamic range. Regardless of intensive theoretical works⁷ and publications of excellent reviews,⁸ the exact nature of the huge

enhancement in Raman intensity found in SERS is still a matter of controversy. The general consensus attributes the observed enhancement to contributions from two mechanisms: one is a long-range electromagnetic effect wherein the local electromagnetic field at or near laser-irradiated noble metal particle surfaces is enhanced as a result of localized surface plasmon excitation, leading to more intense Raman scattering from molecules near or adsorbed onto the particle surfaces, and the other is a short-range chemical effect that involves specific interactions or coupling between analyte molecules and the metal particles.⁹

Over the years, several different techniques have been developed to create or fabricate functional noble metal SERS substrates. The most commonly used substrates are disorganized media, such as metal colloidal films,¹⁰ metal island films on glass,¹¹ electrochemically roughened silver electrodes,¹² or polymer nanoparticles surfaces.¹³ Recent research has led to the syntheses of metal particles with tunable shapes and sizes, such as rods,¹⁴ cubes,¹⁵ and disks,¹⁶ by using chemical reduction reactions in solution; that is, wet chemistry. Typical chemical reducing agents include sodium citrate, sodium borohydride, hydrazine, hydroxylamine hydrochloride, and many others.¹⁷ In most cases, the resultant nanoparticles bear negative surface charge due to the adsorption of negatively charged ions on their surfaces, and hence, they are not the true choice for SERS-based detection of anions due to the unfavorable condition for anion adsorption on the particle surface stemming from elec-

* Corresponding author. E-mail: tpal@chem.iitkgp.ernet.in.

[†] Indian Institute of Technology.

[‡] Sammilani Mahavidyalaya.

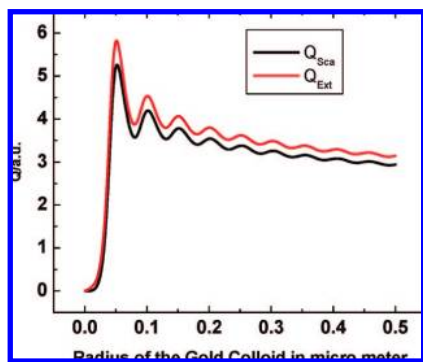


Figure 1. Variation of extinction (Q_{ext}) and scattering (Q_{sca}) efficiencies with the increase in radius of the gold colloid.

trostatic repulsion. As a result, different approaches including surface modification have been performed to render such particles useful for the detection of anions.¹⁸ Recent works by Tan et al.¹⁹ report the synthesis of positively charged silver nanoparticles under UV irradiation. These nanoparticles were also shown to be a superior substrate in SERS detection of thiocyanate, perchlorate, cyanide, and sulfate over commonly used negatively charged citrate-reduced nanoparticles.

Thiocyanate has seen widespread use in electroplating baths and is employed extensively for studies of ionic associations and interactions.²⁰ SCN^- 's bonding with the metals can be classified in three categories: via the S or N end; via both ends in bridge form, and in three-way bridging $\text{M}_2\text{SCN}-\text{M}'$ geometry.²¹ Because of its large infrared and Raman cross section, SCN^- has been studied extensively by different vibrational spectroscopy. Until now, most reported works on SERS involving SCN^- have encompassed the potential-dependent orientation.²² Weaver and co-workers have extensively examined the potential dependency to assess the perturbation in binding mode of this ambidentate anion with change in electrode potential. In addition, the C–N stretching mode, ν_{CN} , has been found to be sensitive to the coordination geometry and environment. On the other hand, methylene blue (MB^+), a potential candidate in photodynamic therapy, has been found to offer promising applications in eradication of viruses, treatment against inoperable esophageal tumors, and in urinary tract infections.^{23a–d} High uptake of MB^+ in cancerous cell cultures has also been observed.^{23e,f} This cationic thiazine dye has a very low fluorescence quantum yield (0.02 ± 0.005) due to a very efficient (0.58) intersystem crossing to triplet state and 3 μs nonradiative decay.²⁴ Considering all the above facts and distinctive features, we have directed our investigation to thiocyanate and also methylene blue as pertinent candidates for observing the SERS under existing different electrostatic field force.

The availability of a range of computational tools allows the experimentalist to use computational methods hand-in-hand with experiment to understand the structural and spectroscopic details of molecules.²⁵ Recently, density functional theory (DFT) has proved to be superior compared to conventional *ab initio* methods in computing quantitative vibrational properties in a cost-effective fashion. Work by Scott and Radom and Wong has shown that DFT predicts harmonic frequencies in excellent agreement with observed fundamentals, having empirical scaling factors close to unity.²⁶ Studies of the vibrational intensities furnished by DFT methods²⁷ lend additional support for the application of DFT in computing reliable theoretical vibrational spectra to assist the interpretation of spectra for unique and complex molecular systems.

In this article, we intend to focus on the query: Is surface enhanced Raman spectroscopy able to investigate the nature of interaction of a probe when it is in different electrostatic environments? The experimental results leaves a “yes” signature. When SERS of thiocyanate is executed in gold sols encompassing positive and negative surface charge, distinguishable results are obtained. The positively charged surface is observed to be a better platform than the negative one in bringing interaction with negatively charged SCN^- . An Analogous conclusion can be drawn for MB^+ when we observed a more enhanced SERS spectrum in a negative colloid. However, fluorescence quenching of 1-methylaminopyrene (MAP) could not be accounted for in light of an electrostatic field force because of the distance-dependence effect. There are only a few reports on theoretical calculations on SERS of SCN^- ,²⁸ so to gain further insight into the interaction, DFT calculations were carried out at the B3LYP/Lanl2DZ level on the basis of five different molecule/metal interaction models. This approach allows us to quantitatively furnish detailed information relating the vibrational properties of thiocyanate and the nature of the nanoparticles–adsorbate bonding.

2. Experimental Section

2.1. Materials. All the reagents used were of AR grade and were used as received without further purification. Amberlite IRA-410 CL resin ($\text{C}_{13}\text{H}_{20}\text{NO} \cdot \text{C}_{10}\text{H}_{10} \cdot \text{Cl}$)_x, chloroauric acid ($\text{HAuCl}_4 \cdot 3\text{H}_2\text{O}$), and 1-methylaminopyrene were purchased from Aldrich. Trisodium citrate ($\text{Na}_3\text{C}_6\text{H}_5\text{O}_7$), cetylpyridinium chloride (CPC) and ammonium thiocyanate (NH_4SCN) were purchased from Merck, India. Methylene blue was purchased from S.d.fine Chem. Ltd. All glassware were cleaned using aqua regia, subsequently rinsed with a copious amount of double distilled water, and dried well prior to use.

2.2. Preparation of Gold Sol by the Frens's Method. Gold colloid of size ~ 55 nm was prepared by the well-documented traditional Frens's method.²⁹ In brief, a 50 mL aqueous solution of HAuCl_4 (2.5×10^{-3} M) was heated to boiling; 0.4 mL of trisodium citrate solution (1% by wt) was then added to it under continuous stirring. Within 20 s of boiling, the solution turned faint blue (nucleation); under continuous stirring condition, after 50 s, the blue color suddenly changes to pinkish-red, indicating the formation of gold nanoparticles. The reaction mixture was boiled for another 30 min for complete reduction of the Au(III) ions. The solution was set aside to cool to room temperature. Absorption measurement of the finally formed gold colloid showed an intense absorption band with a maximum at 529 nm. The gold nanoparticles synthesized in this way were negatively charged because these were exchangeable with anion-exchange resin.

2.3. Immobilization and Recovery of the Gold Nanoparticles onto and from the Anion Exchange Resin. In a conical flask, ~ 0.5 g of resin beads were soaked overnight in water. Any impurity in the resin particles could cause gold particles aggregation, so the beads were washed several times with water before immobilization. Then ~ 50 mL of the freshly prepared citrate-capped gold sol was added in portions (i.e., in small aliquots) (5 mL) for complete immobilization of the gold nanoparticles in resin matrix to avoid the difficulty of aggregation resulting from the expelled Cl^- . After each step, the supernatant became colorless, and the beads were washed with water to wash out the expelled Cl^- . A gradual change in color of the resin beads from yellow to black substantiates the completion of the binding process. The resin beads were further washed with plenty of water. For the recovery of the Au nanoparticles from the resin beads, aqueous CPC (50 mM)

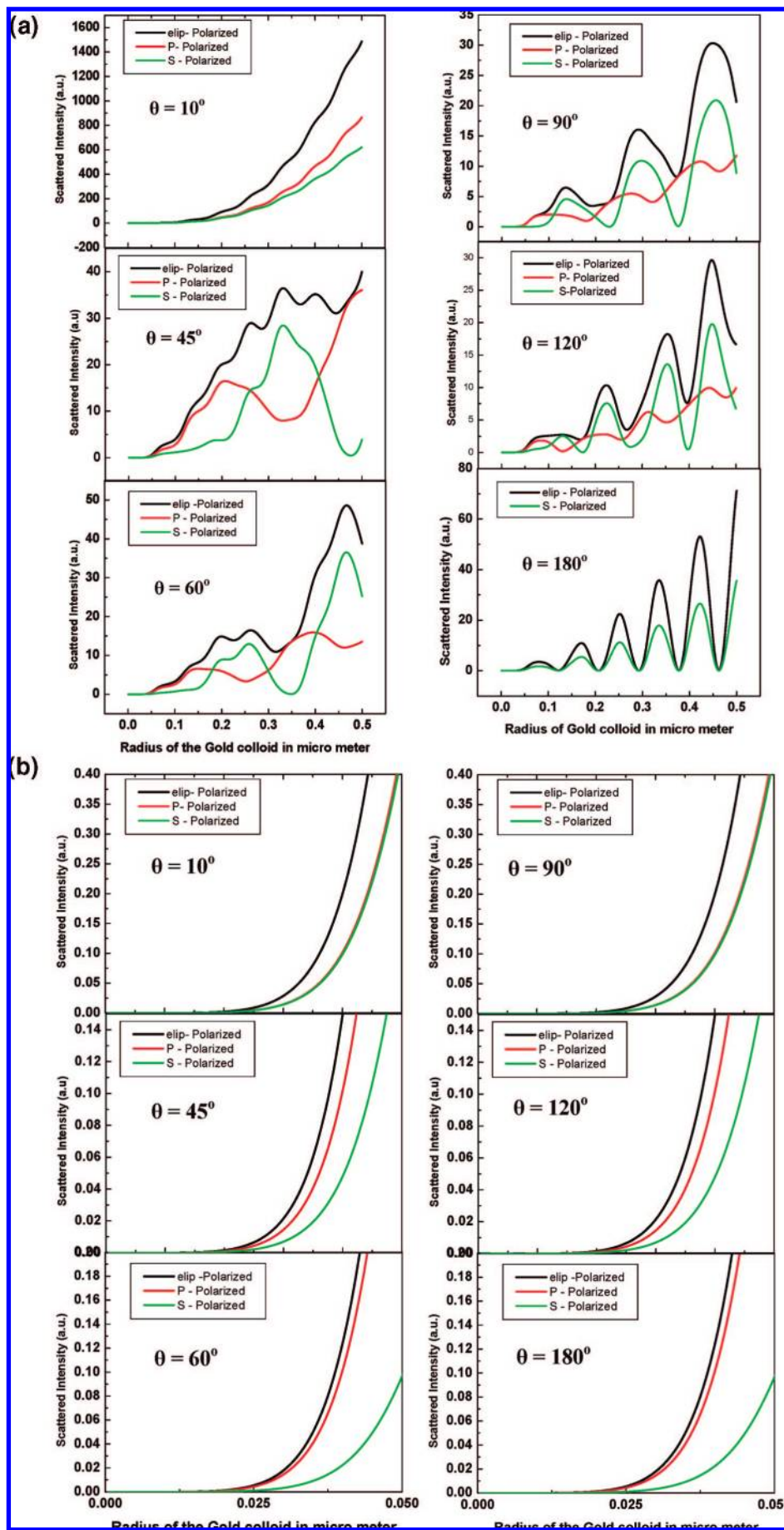


Figure 2. Variation of the scattered intensity of e-, s-, and p-polarized light with the increase in radius of the gold colloid at various angles of scattering (for $\lambda = 633$ nm) in the range of (a) 0–0.50 and (b) 0–0.050 μm particle size.

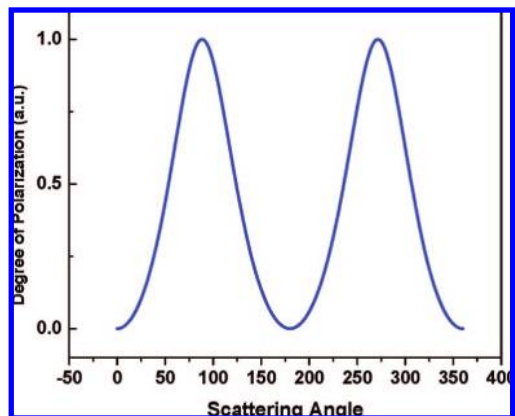


Figure 3. Variation of the degree of polarization with the scattering angle (for $r = 30$ nm and for $\lambda = 633$ nm).

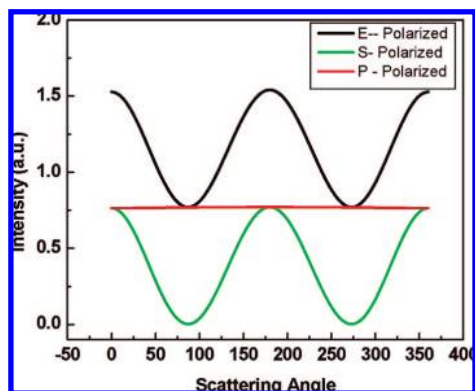


Figure 4. Variation of the scattered intensity of e-, s-, and p-polarized light from a spherical gold colloidal particle of radius ~ 30 nm with the angle of scattering (for $\lambda = 633$ nm).

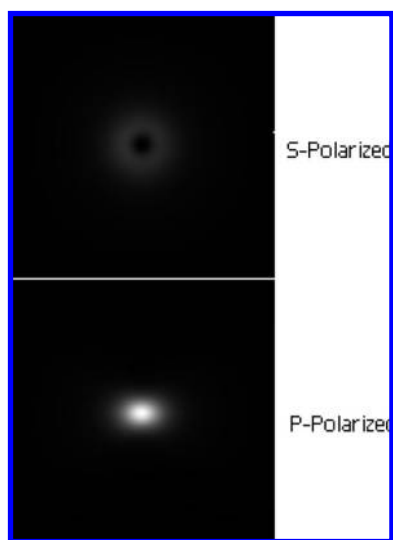


Figure 5. The spatial distribution of the near field at scattering angle $\theta = 120^\circ$ for an isolated gold colloidal particle of radius $r \sim 30$ nm (for $\lambda = 633$ nm).

solution was added in portions of ~ 2 mL at the respective stages. The solution above the resin became pinkish-violet instantaneously, indicating the recovery. The Au nanoparticles in this recovered solution were exchangeable with cation exchange resin, R^+H^+ , but not with anion exchange resin, which signifies that the surface charge of these nanoparticles were positive. The resin beads obtained after recovery of the gold were washed thoroughly with water and were reusable.

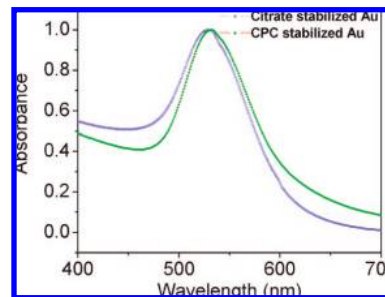


Figure 6. UV-vis absorption spectra of citrate and CPC-stabilized gold colloids.

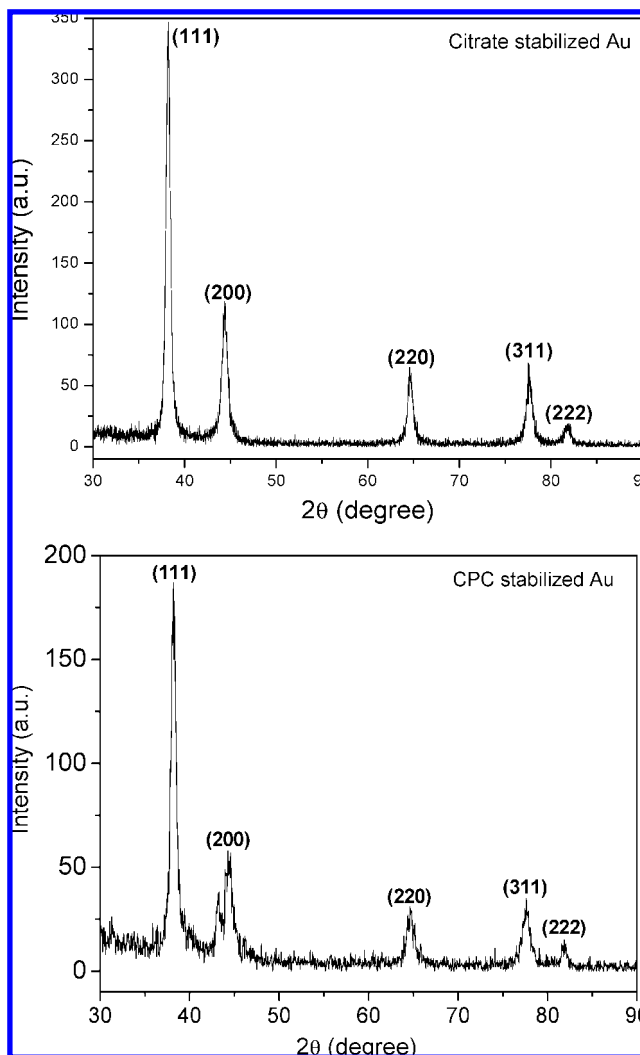


Figure 7. Powder X-ray diffraction pattern of citrate and CPC-stabilized gold colloids.

2.4. Analytical Measurements. 2.4.1. UV-Visible Spectroscopy. Absorption spectra were recorded in a Spectrascan UV 2600 spectrophotometer (Chemito, India), and the solutions were taken in a 1 cm well-stoppered quartz cuvette.

2.4.2. Fourier Transform Infrared Spectroscopy (FTIR). FTIR spectral characteristics of NH_4SCN were collected in a KBr pellet in reflectance mode with a Nexus 870 Thermo-Nicolet instrument coupled with a Thermo-Nicolet Continuum FTIR microscope.

2.4.3. X-ray Diffraction (XRD) Study. XRD patterns of the products were recorded on a Philips PW-1710 X-ray diffractometer (40 kV, 20 mA) using Cu $K\alpha$ radiation ($\lambda = 1.5418$ Å) in the 2θ range of 30 – 90° .

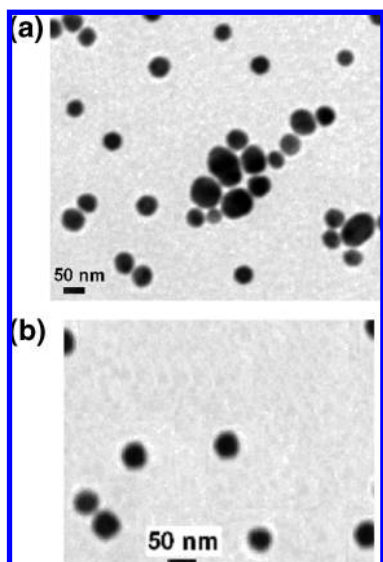


Figure 8. TEM images for 55 nm gold nanoparticles stabilized by (a) citrate and (b) CPC.

2.4.4. Transmission Electron Microscopy (TEM). TEM was carried out on a Hitachi H-9000 NAR transmission electron microscope operating at 100 kV. Samples were prepared by placing a drop of solution on a carbon-coated copper grid, followed by solvent evaporation in vacuo.

2.5. Fluorescence Measurement. Fluorescence spectra were recorded with a Perkin-Elmer LS-55 spectrofluorimeter equipped with a 20 kW xenon discharge lamp and a photo multiplier tube with S-5 spectral response. The spectrofluorimeter was linked to a personal computer and utilized the Perkin-Elmer FL Winlab software package for data collection and processing. An excitation wavelength of 278 nm and slit width 2.5/2.5 nm were used to record the spectra.

2.5.1. Preparation of Gold Probe Assembly for Fluorescence Measurement. In a typical set, a known amount of gold was added to an aqueous solution of MAP, and the final volume of the solution was maintained at 4 mL in 1 cm well-stoppered quartz cuvettes. The final concentration of MAP was 10^{-7} M. The solutions were allowed to stand for ~ 6 h for the completion of the surface complexation process between the gold nanoparticle surfaces and the probe. Finally, fluorescence of each solution was measured in the spectrofluorometer.

2.6. SERS Measurement. Raman spectrum of the samples were obtained with a Renishaw Raman microscope equipped with a He–Ne laser excitation source emitting at a wavelength of 632.8 nm and a Peltier cooled (-70 °C) charge-coupled device (CCD) camera. A Leica DMLM microscope was attached and was fitted with three objectives (5 \times , 20 \times , 50 \times). For our experiments, the 20 \times objective was used. Laser power at the sample was 15 mW, and the data acquisition time was 30 s. The holographic grating (1800 grooves/mm) and the slit provided a spectral resolution of 1 cm^{-1} .

2.6.1. Preparation of the Samples for Surface-Enhanced Raman Scattering. Two milliliters of the gold sols (both citrate and CPC-stabilized) were taken in two separate glass vials. A 0.5 mL portion of the aqueous solution of the probe molecule (NH_4SCN) was added to the Au sol separately. A similar step was followed for the SERS measurement of MB^+ . Final concentrations of NH_4SCN and MB^+ in the incubated solutions were 10^{-4} and 10^{-5} M, respectively. A 15 μL portion of each of the above solutions was dropped onto the glass substrate, and SERS measurements could be started as soon as the solvent evaporated.

3. Computational Details

The Mie theory calculations were performed using Scat Lab1.2 software for gold nanoparticles of diameter ~ 60 nm. However, the limitations of the software restrict us to calculate the optical properties of the nanoparticles below ~ 60 nm diameter. The average particle size of the gold nanoparticle is ~ 55 nm, and the size distributions of the nanoparticles are spread in the range of 50–60 nm. So the numerical calculation of the optical properties of the nanoparticles with ~ 60 nm diameter is expected to reflect a qualitative idea concerning the optical properties of the nanomaterials in the above-mentioned range of particle size distribution. All density functional theory calculations were carried out using the Gaussian 03 program for Windows³⁰ for optimization of the molecular structures and calculations of the vibrational frequencies for the optimized structures. The B3LYP, that is, Becke three-hybrid exchange,³¹ and Lee–Yang–Parr correlation functional (LYP),³² were utilized in the DFT calculations with the Pople split valance polarization basis set 6-31G(d,p) and Lanl2DZ basis set^{33a} for free molecules. These two basis sets do not lead to significant differences in the measurement of the structural parameter of the molecule. However, significant variations are observed in the estimation of the vibrational frequencies of the molecule. The variation in the prediction of vibrational frequencies by these two basis sets is a well-known phenomenon and has been reported elsewhere.^{33b,c} However, for the molecule–metal model complexes, the geometry optimization was fruitful using only the Lanl2DZ basis set. In addition, the theoretically estimated vibrational frequencies obtained from the B3LYP/Lanl2DZ level of calculations satisfactorily agree with the calculated and the observed vibrational frequencies apart from/without using a scaling factor. The unique choice of the Lanl2DZ basis set in the DFT calculations thus allows one to compare the ground-state optimized geometries of the free and surface-adsorbed molecule. In the process of geometry optimization for the fully relaxed method, convergence of all of the calculations and the absence of imaginary values in the wave numbers confirmed the attainment of local minima on the potential energy surface. Cartesian displacement and calculated (B3LYP/Lanl2DZ) vibrational modes of the molecule have been displayed using Gauss View-03 software. The potential energy distributions (PED) calculation was performed with GAR2PED³⁴ in terms of internal coordinates of the molecule from the output of the DFT calculations. The observed disagreement between the theory and the experimental results could be a consequence of the anharmonicity and also may be due to the general tendency of the quantum chemical methods to overestimate the force constants at the exact equilibrium geometry.³⁵ However, it is emphasized that the calculated Raman spectrum represents the vibrational signatures of molecules in the gas phase. Hence, the experimentally observed normal Raman spectrum (NRS) of solid and solution may differ significantly from the calculated spectrum.³⁶ Despite this fact, it is observable that there is a general concordance regarding the Raman intensities as well as the position of the peaks between the experimental and calculated spectra.³⁷

4. Results and Discussion

4.1. Evolution and Characterization of Gold Colloidal Solution. **4.1.1. Optical Properties of the Synthesized Gold Nanoparticles; an Account from Mie Theory.** The synthesis of 55 nm gold nanoparticles has been exploited as the SERS substrate. The particles bear a tight size distribution, and Mie theory was applied for obtaining scattering parameters for the

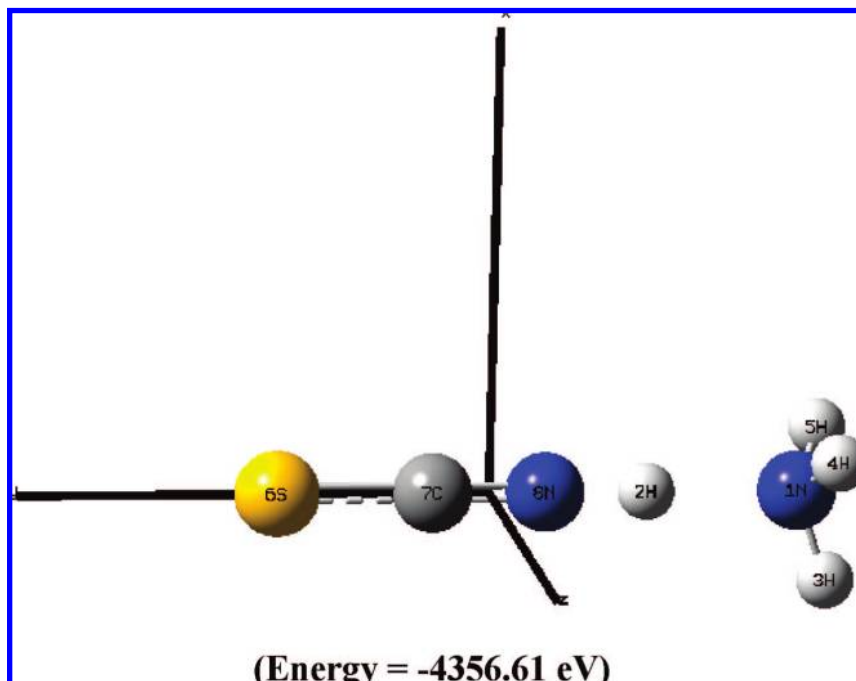


Figure 9. Optimized molecular structure and energy of NH_4SCN from the B3LYP/Lan12DZ level of theory.

TABLE 1: Relevant Structural Parameters of NH_4SCN Calculated from the B3LYP/Lan12DZ and B3LYP/6-31G (d,p) Level of Theory

Lan12DZ			
before adsorption	after adsorption	shift (Δ)	6-31G (d,p)
Bond Length (\AA)			
S6-C7, 1.651	S6-C7, 1.725	0.074 (increased)	S6-C7, 1.654
C7-N8, 1.194	C7-N8, 1.184	0.009 (decreased)	C7-N8, 1.185
H3-N8, 1.075			H2-N8, 1.069
N1-H3, 1.597			N1-H2, 1.609
N1-H2, 1.020			N1-H3, 1.016
N1-H4, 1.020			N1-H4, 1.016
N1-H5, 1.020			N1-H5, 1.016
Bond Angle (deg)			
H2-N1-H3, 108.5			H2-N1-H3, 107.9
H2-N1-H4, 110.5			H2-N1-H4, 107.9
H2-N1-H5, 110.5			H2-N1-H5, 107.9
H3-N1-H4, 108.4			H3-N1-H4, 110.9
H3-N1-H5, 108.4			H3-N1-H5, 110.9
H4-N1-H5, 110.5			H4-N1-H5, 110.9

particles with the idea of ray optics in relation to the variable scattering angles.^{38a} Both positive and negatively charged gold particles were spherical and monodispersed in the aqueous medium, with average particle size ~ 55 nm diameter (Figure 8). For an isolated spherical particle (irrespective of surface

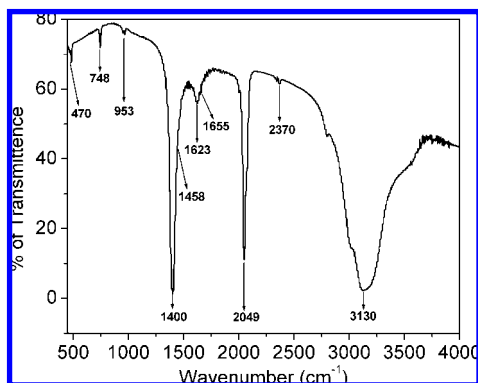


Figure 10. FTIR spectrum of NH_4SCN .

charge) of arbitrary radius and optical constants illuminated by electromagnetic radiation of a given wavelength, Mie theory allows one to estimate the scattering (Q_{sca}) and extinction efficiencies (Q_{ext}), where extinction is the removal of light from the incident beam by absorption and scattering.

The scattering (Q_{sca}), absorption (Q_{abs}) and extinction (Q_{ext}) efficiencies are expressed as:

$$Q_{\text{sca}} = \frac{2}{x^2} \sum_{n=1}^{\infty} (2n+1) (|a_n|^2 + |b_n|^2)$$

$$Q_{\text{ext}} = \frac{2}{x^2} \sum_{n=1}^{\infty} (2n+1) [\text{Re}(a_n + b_n)]$$

$$Q_{\text{abs}} = Q_{\text{ext}} - Q_{\text{sca}}$$

where n is the summation index of the partial waves; $n = 1$ corresponds to the dipole oscillation, $n = 2$ is associated with the quadrupole oscillation, and so on; a_n and b_n are the Mie coefficients and are functions with numerous poles in the complex plane. The Mie coefficients a_n and b_n can be evaluated with complex Bessel–Riccati functions Ψ and ζ using the following relations:

$$a_n = \frac{\psi'_n(mx) \psi_n(x) - m \psi_n(mx) \psi'_n(x)}{\psi'_n(mx) \xi_n(x) - m \psi_n(mx) \psi'_n(x)}$$

$$b_n = \frac{m \psi'_n(mx) \psi_n(x) - \psi_n(mx) \psi'_n(x)}{m \psi'_n(mx) \xi_n(x) - \psi_n(mx) \xi'_n(x)}$$

$m = n_p/n_m$, where n_p denotes the complex index of refraction of the particle, n_m is the real index of refraction of the surrounding medium, and x is the size parameter and is expressed as $x = 2\pi n_a r/\lambda$.

The Mie theory has been applied to elucidate the variations of scattering/extinction cross section and intensity of scattered radiation with the size of the gold colloidal particles at various scattering angles. The variations are shown graphically in Figures 1 and 2. The theory has been further applied to estimate

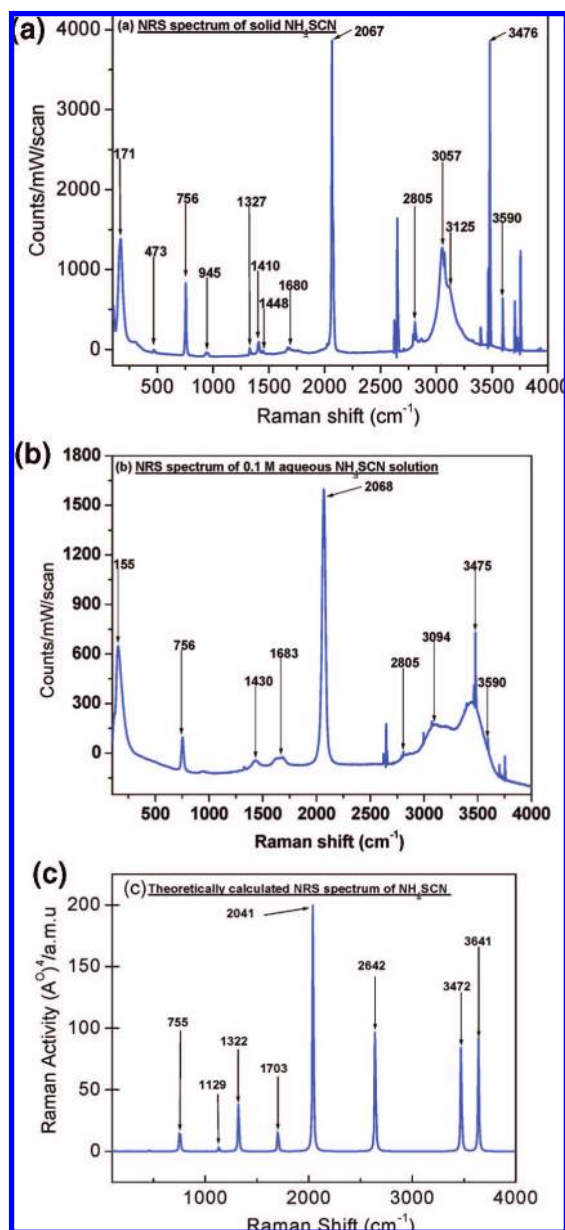


Figure 11. Normal Raman spectrum of NH_4SCN (a) in the solid state and (b) in a 0.1 M aqueous solution for $\lambda_{\text{exc}} = 632.8$ nm. (c) The theoretical gas-phase Raman spectrum of NH_4SCN calculated using B3LYP/Lan12DZ level of theory.

the degree of polarization and scattering intensity with the variation in the scattering angle (Figures 3 and 4). The nonabsorbing materials have real values of the refractive index, whereas the absorbing materials have complex values of the refractive index. The nanomaterials have strong plasmon absorption in the visible region of the electromagnetic spectrum, and hence, the complex value of the refractive index has been selected. In the above-mentioned calculations, the complex refractive index (n_p) for a gold colloidal particle of ~ 30 nm radius (to obtain qualitative information, we used the Scat Laboratory 1.2 software with which we could not go below ~ 30 nm radius) and the real refractive index of the surrounding aqueous medium are taken as $0.183\ 604\ 1 + i\ 3.432\ 260\ 7$ and $1.331\ 613\ 0$, respectively, for a wavelength of incident radiation $\lambda = 633$ nm.^{38b,c}

In the visible region of the electromagnetic spectrum, the refractive index of water has a very small imaginary component, ca. $1.332\ 57 + 0.000\ 000\ 016\ 4i$, at a wavelength of $0.65\ \mu\text{m}$.

In practice, the imaginary component is usually ignored for the sake of calculations of scattering from water, thus assuming that water is nonabsorbing.^{38d} In the present context, the refractive index of the surrounding aqueous medium is thus considered to have a real value. From Figure 1, it is seen that the extinction and the scattering efficiency approach limiting values as the radius of the gold colloidal particles increases. The above variation of the scattering and absorption efficiency with the radius of the gold colloidal particles can be explained from the view of geometrical optics. The total extinction is due to the redistribution of incident rays because of diffraction about the edge of the spherical gold colloidal particle, specular reflection at the surface, and refraction into the sphere. The refracted rays, which undergo successive internal reflections within the sphere and refractions out of the sphere, are attenuated while passing through the absorptive material. If the spherical colloidal particle is sufficiently large and if the material is sufficiently absorptive, most of the radiation refracted into the sphere will be absorbed and, thus, will represent the absorption efficiency.

The plane of observation is defined by the plane containing the direction of the incident beam of radiation and the direction of observation. In the case of natural (unpolarized) light, the incident beam of the scattered radiation in the plane of observation is generally expressed by two intensity functions, $I(\perp)$ and $I(\parallel)$, for the two cases of the electric field vector vibrating perpendicular and parallel, respectively, to the plane of observation. These intensity functions are given by

$$I(\perp) = |T_1(\theta)|^2$$

$$I(\parallel) = |T_2(\theta)|^2$$

where $T_1(\theta)$ and $T_2(\theta)$ are the scattering amplitude functions which determine the intensity and the state of polarization of the scattered radiation in any direction specified by the scattering angle, θ . θ is defined as the angle between the direction of the scattering and the propagation vector of the incident radiation. The degree of polarization of the scattered beam is given by

$$P = \frac{I(\perp) - I(\parallel)}{I(\perp) + I(\parallel)}$$

Figure 3 shows the calculated variation of P with the scattering angle θ using Mie theory. The radiation incident on the sphere may have an arbitrary intensity and state of polarization. Generally, the scattered radiation is elliptically polarized, even if the incident beam has linear polarization, because $T_1(\theta)$ and $T_2(\theta)$ are complex quantities with differing phases. However, the scattered light can be linearly polarized when the plane of observation is parallel or perpendicular to the direction of the electric vector in the incident beam of light.

The theoretically estimated variation of the scattered radiation for the e-, s-, and p-polarized light for the gold colloid of 30 nm radius with the angle of scattering is shown in Figure 4.

Figure 2a shows the theoretically simulated variation of the scattered intensity of e-, s-, and p-polarized light with an increase in the radius of the gold colloidal particles at different angles of scattering. Figure 2b also shows the same variation of the scattered intensities with an increase in the radius of the gold nanoparticles, specifically in the range of $0\text{--}0.050\ \mu\text{m}$ particle size. At low scattering angle (ca. $\theta = 10^\circ$), the intensity of the scattered radiations emerge as broad and diffused humps which at the higher scattering angles (ca. $\theta = 45^\circ$ and 60°) appear as ripples and distinct overlapped peaks. At scattering angles $\theta \geq 90^\circ$ the broad and overlapped humps appear as discrete peaks

TABLE 2: Observed and Calculated Raman and FTIR Bands of NH₄SCN with Their Tentative Assignments^a

FTIR (obs/cm ⁻¹)	NRS solid (obs/cm ⁻¹)	NRS solid (calc/cm ⁻¹)		NRS soln (cm ⁻¹)	tentative assignments (PED %)
		Lanl2DZ	6-31G (d,p)		
		3641ms	3639		61r _{1,3} 32r _{1,5}
		3472ms	3476		33r _{1,5} 33r _{1,3} 33r _{1,4}
3130sb		2642ms	2668		79r _{2,8} 13r _{7,8} 7r _{1,2}
2370vww					
2049s	2067vs	2041vs	2077	2068vs	59r _{7,8} 26r _{2,8} 9r _{6,7} 5r _{1,2}
1655vww	1680vww	1703w		1683vww	78α _{3,5,1} 21α _{3,4,1}
1458vww	1448vww			1430vww	
1400vs	1410vw				
	1327vww	1322m			44(β _{out}) _{1,8,2,1} 19(β _{in}) _{1,8,2,1} 17α _{5,2,1} 9(β _{out}) _{2,7,8,1} 7α _{4,2,1}
			1215		
		1129vww	1118		94α _{4,5,1}
748vw	756ms	755w	752	756m	78r _{6,7} 10r _{1,2} 7r _{7,8} 6r _{2,8}
470vw	473vww	461			52(β _{out}) _{8,6,7,1} 20(β _{in}) _{8,6,7,1} 10(β _{out}) _{2,7,8,1} 7α _{4,2,1}
		415	430		44α _{5,2,1} 18(β _{out}) _{1,8,2,1} 17α _{4,2,1} 8(β _{out}) _{8,6,7,1} 7(β _{in}) _{1,8,2,1}
			381		
		270	267		88r _{1,2} 10r _{2,8}
	171ms			155ms	
		76			49(β _{in}) _{2,7,8,1} 20(β _{in}) _{1,8,2,1} 18(β _{out}) _{2,7,8,1} 8(β _{out}) _{1,8,2,1}

^a r, stretching; α, in-plane bending; β_{in}, in-plane linear bending; β_{out}, out-of-plane linear bending; sb, strong and broad; s, strong; vs, very strong; ms, medium strong; w, weak; vw, very weak; vww, very very weak. Only contributions ≥ 5 are reported.

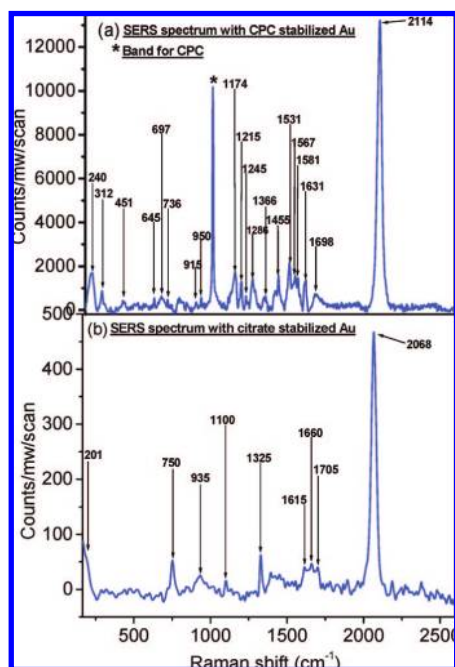


Figure 12. SERS spectra of NH₄SCN at a concentration of 10⁻⁴ M with (a) CPC- and (b) citrate-stabilized Au colloid.

with the disappearance of ripples. In general, the scattered light intensities (for e-, s-, and p-polarized light) at various scattering angles progressively increase with the radius of the gold colloidal particle, which can also be explained from the view of ray optics. The scattering at low angles ($\theta < 90^\circ$) is mostly confined in the forward direction, and the appearance of diffused, broad, and overlapped humps in the scattered intensity plot can be interpreted as due to the interference of a specularly reflected ray, rays due to surface waves, and also due to diffraction whose localization predominantly increases with the size of the colloidal particles. At higher scattering angles ($\theta > 90^\circ$), the scattering intensity can be interpreted as due to the interference between a specularly reflected ray and rays sprayed as the surface waves. With an increase in the scattering angle, the interference from the diffracted rays decreases and becomes a

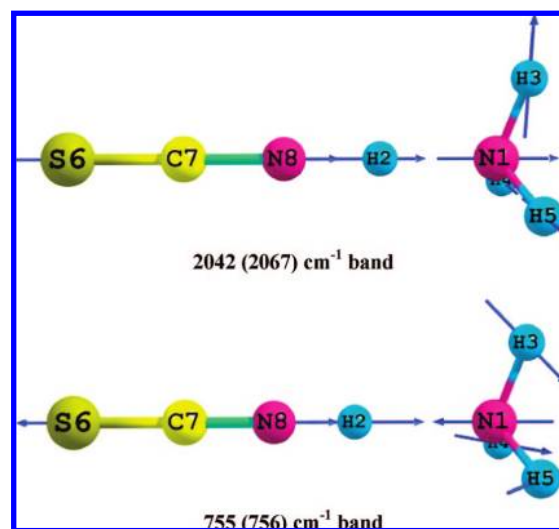


Figure 13. Cartesian displacement and calculated (B3LYP/Lanl2DZ) vibrational modes of NH₄SCN. The numbers in the parentheses refer to the experimental value of the assigned band.

minimum at $\theta = 180^\circ$. This may result in the appearance of sharp peaks in the intensity plot of the colloidal gold particles whose amplitude progressively increases with the radius of the colloidal particles. The interference from the surface and diffracted waves (only for low scattering angles) also predominantly increases with an increase in radius of the colloidal particles. This may result in an increase in scattered intensity of the e-, s-, and p-polarized light with an increase in the radius of the colloidal particles also for the scattering angle $\theta \leq 90^\circ$. The spatial distribution of the near field intensity at $\theta = 120^\circ$ for the s- and p-polarized scattered light is shown in Figure 5.

4.1.2. Immobilization and Recovery of Gold Nanoparticles onto and from Anion Exchange Resin. The gold sol prepared by Frens's method bears a negative surface charge³⁹ because of capping by the unreacted citrate ions, and thus, they are readily exchangeable by anion-exchange resin. The Cl⁻ ions thus expelled from the resin after exchange would cause aggregation of gold nanoparticles due to electrolytic effect. So after each step of immobilization, washing of the beads with

TABLE 3: Observed SERS Bands of the Molecule (NH₄SCN) on Positive and Negatively Charged Au Colloid and Apparent Enhancement Factor (AEF)

positively charged Au colloid		negatively charged Au colloid	
SERS	AEF	SERS	AEF
2114s	7.9×10^3	2068s	2.75×10^2
1698vw		1705vvw	
		1660vvw	
1631w		1615vvw	
1581vvw			
1567vvw			
1531w			
1455w			
1366vw		1325vvw	
1286w			
1245vvw			
1215vw			
1174w			
		1100vvw	
950vvw			
915vvw		935vw	
736vvw		750w	
697vvw			
645vvw			
451vw			
312vw			
240w			
		201vvw	

water was necessary. We discovered that an aqueous solution of a cationic surfactant (CPC) has been used for the quantitative retrieval of the gold nanoparticles from the resin bead to the solution.⁴⁰ This surfactant not only efficiently eluted the gold nanoparticles but also provides an in-house stability, presumably through the attachment of the pyridinium ring containing a long hydrocarbon chain through its nitrogen (present as N⁺) on the eluted gold surface in a perpendicular manner.⁴¹ The ready exchange of these CPC-stabilized gold hydrosol in cation exchange resin (Dowex-50) substantiated the positive surface charge of these nanoparticles.

4.1.3. Absorption Spectra. Figure 6 illustrates the UV–visible spectra of citrate and CPC-stabilized gold nanoparticles in solution. Citrate-stabilized gold sol shows absorption maxima (λ_{max}) at 529 nm, whereas for CPC-stabilized sol, the λ_{max} value is red-shifted (533 nm). These colloidal solutions were stable for a couple of days without observable aggregation under ambient conditions, as confirmed by UV–visible analysis.

4.1.4. Powder X-Ray Diffraction Pattern. The as-prepared gold sol (both citrate- and CPC-stabilized) was centrifuged, and the centrifugate obtained was spotted on a glass slide. Thereafter, both the slides were dried under vacuum and taken for XRD analysis. The patterns recorded from the samples prepared are displayed in Figure 7, and the peaks at $2\theta = 38.23, 44.35, 64.57, 77.55,$ and 82.07° (for citrate-stabilized gold) were assigned to be the diffraction from the {111}, {200}, {220}, {311}, and {222} facets, respectively, of the fcc crystal structure of gold.⁴² For CPC stabilization there was practically no alteration in the diffraction pattern. 2θ values in this case are $38.17, 44.57, 64.62, 77.62,$ and 82.02° for the respective planes, as in the above sequence. This feature clearly depicts the fact that the crystallinity of the gold nanoparticles remains unaltered for both kind of stabilization. The XRD pattern shows broad bands for the {111} and {200} reflections for the gold nanoparticles. These broad peaks are characteristic of metal colloidal clusters owing to the very small size of the particles.⁴³ This result is similar to that reported by Leff et al. for long-chain alkylthiol passivated gold nanoparticles.⁴⁴ Here, it is worth mentioning that the ratio

between the intensities of the {200} and {111} diffraction peaks is lower than the conventional value (0.343 versus 0.53 for citrate-stabilized; 0.304 versus 0.53 for CPC-stabilized). The ratio between the intensities of the {220} and {111} peaks is also much lower than the conventional value (0.187 versus 0.33 for citrate-stabilized; 0.166 versus 0.33 for CPC-stabilized), both indicating that our nanoparticles were abundant in {111} facets, and thus, their {111} planes tend to be preferentially oriented (or textured) parallel to the surface of the supporting substrate.⁴⁵

4.1.5. TEM Image. From the TEM images in Figure 8, it is evident that the citrate-stabilized gold sol does not show any momentous change in the size and shape of the Au nanoparticles from that of CPC-stabilized sol. Therefore, it is definite that the employment of the surfactant in the elution process results only in a positional shift in the gold plasmon absorption band.

4.2. Application of Synthesized Gold Colloids as Active Materials in SERS. **4.2.1. Raman and SERS Spectra of Thiocyanate (SCN⁻).** The adsorption of thiocyanate on metal surfaces is of particular interest because this molecule presents ambidentate functionality with the possibility of either N or S or both N and S coordination. In this article, we have exploited SERS as a spectroscopic tool to investigate the fate of surface charge of colloidal metal (Au) nanoparticles for their interaction with probe molecules, SCN⁻. Keeping the success of DFT in computation of vibrational frequencies and elucidation of structural details in mind, this theory has been utilized here to model the experimentally observed NRS and SERS spectra.

The optimized molecular structure of ammonium thiocyanate (considering its C_s symmetry) is shown in Figure 9. The corresponding energy at global minima of the potential energy surfaces of the molecule is also shown in Figure 9. Table 1 shows the selected optimized structural parameters and rotational constant of the molecule. The theoretical results estimated from the DFT calculations for thiocyanate moiety are almost comparable with the reported crystallographic data of several thiocyanate–metal complexes when compared with the ligand, thiocyanate.⁴⁶

The FTIR spectrum of NH₄SCN is given in Figure 10. The corresponding normal Raman spectrum of the neat solid and its 0.1 M solution are depicted in Figure 11a and b, respectively. The simulated normal Raman spectrum of the molecule in the gas phase is shown in Figure 11c. Table 2 lists the experimentally observed FTIR and NRS band frequencies of the molecule. The theoretically computed vibrational frequencies of the molecule in the gas phase are also shown in Table 2, along with their tentative assignments, as provided from the potential energy distributions. The FTIR spectrum and the normal Raman spectrum of the sample have been characterized by sharp and well-resolved vibrational bands, and these observed vibrational signatures are harmonized with the theoretically computed one. Interesting observations have been identified regarding the appearance of a band at around $\sim 2068 \text{ cm}^{-1}$. This mode is intense and strongly polarized in the NRS spectra and has a prevailing contribution from the in-plane C₇–N₈ stretching vibration of the molecule. However, the DFT and PED calculations further suggest that this band may also represent vibrational signatures having significant contribution from in-plane C₇–S₆ and N₈–H₂ stretching vibrations. The FTIR counterpart of this band appears at 2049 cm^{-1} . The band at $\sim 756 \text{ cm}^{-1}$ has been assigned to the C₇–S₆ stretching vibration. The out-of-plane H₄–H₂–H₅–N₁ bending mode also imparts contribution to this frequency. Another vibrational band, emanating from the thiocyanato part of the molecule, is observed at $\sim 473 \text{ cm}^{-1}$, which has no counterpart in the NRS spectrum

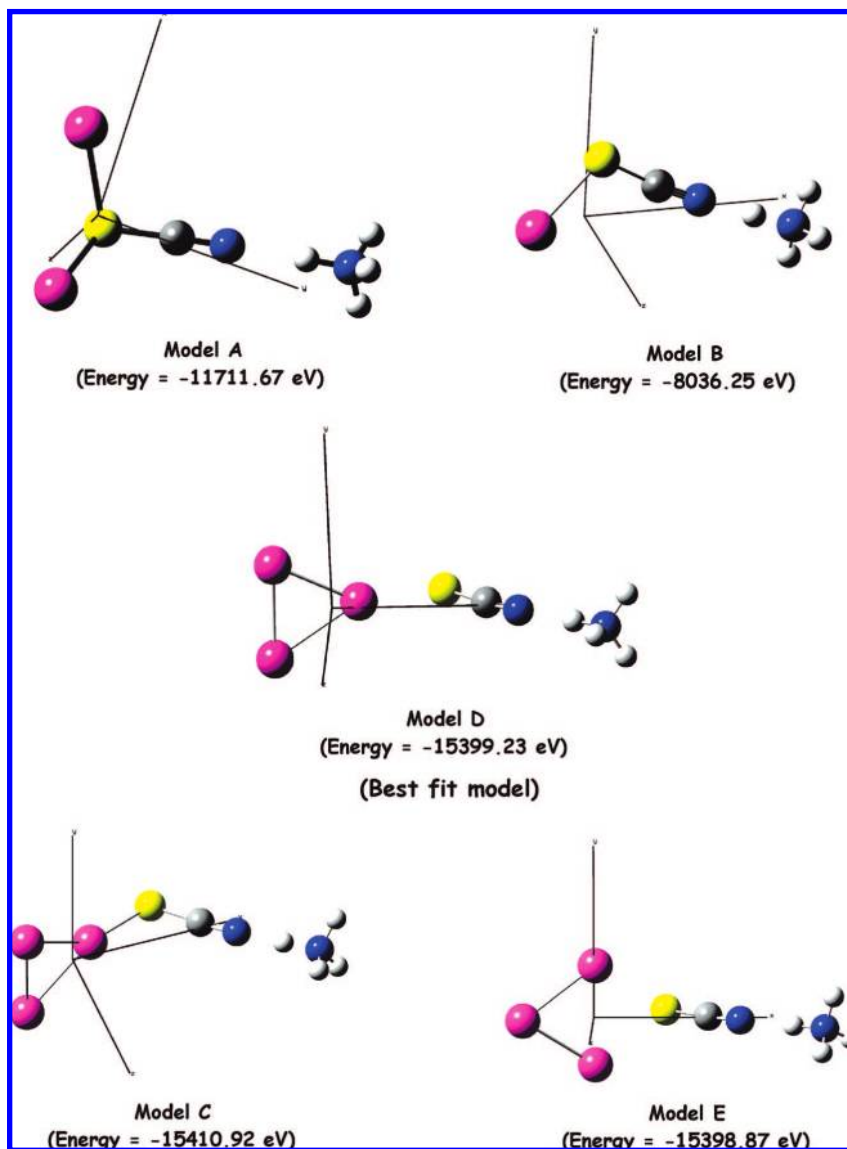


Figure 14. Optimized molecular structures of five different Au–thiocyanate interaction models with their respective BSSE-corrected energy values (color scheme for atoms: pink, gold; yellow, sulfur; blue, nitrogen; black, carbon; light gray, hydrogen).

of the molecule recorded in the solution, but does have in FTIR at $\sim 470\text{ cm}^{-1}$. This band has a dominant contribution from in-plane $\text{N}_8\text{--S}_6\text{--C}_7$ bending. Similarly, the band at $\sim 1327\text{ cm}^{-1}$ has major contributions from in-plane $\text{N}_8\text{--H}_2\text{--C}_7$ bending and appears only in the NRS of the solid sample.

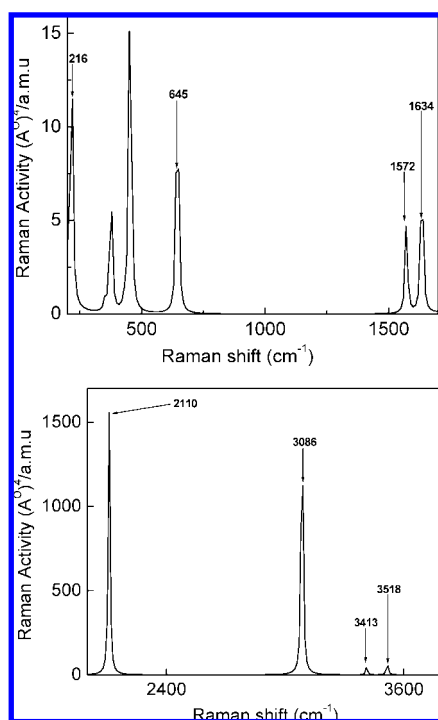
The SERS spectrum at 10^{-4} M adsorbate concentration shows significant changes as compared to the NRS spectrum of thiocyanate (Figure 12). Considerable attention can be drawn to the band centered at $\sim 2068\text{ cm}^{-1}$ in the SERS spectra of citrate-stabilized gold (negatively charged surface) colloid (Figure 12b). This band, ascribed to the in-plane $\text{C}_7\text{--N}_8$ stretching vibration of the molecule, is considerably blue-shifted by $\sim 46\text{ cm}^{-1}$ (appears at $\sim 2114\text{ cm}^{-1}$) and significantly enhanced in intensity in the SERS spectra of CPC-stabilized gold (positively charged surface) colloid (Figure 12a). Apart from this mode, the remaining intramolecular modes, C–S stretching (ν_{CS}) and N–C–S bending (δ_{NCS}), are also discernible by SERS.⁴⁷ The band at $\sim 756\text{ cm}^{-1}$ (ν_{CS}) in NRS as well as in a simulated spectrum shows its very weak signature at $\sim 736\text{ cm}^{-1}$ for CPC gold sol, although this band retains its position unchanged for citrate gold sol. The Cartesian displacements of the above-mentioned vibrations have been represented in Figure

13. Similarly the band at $\sim 473\text{ cm}^{-1}$ (δ_{NCS}) in NRS is slightly red-shifted in SERS and appears at $\sim 451\text{ cm}^{-1}$ as a weak band for CPC-stabilized gold sol, whereas this mode completely disappears in the case of citrate-stabilized gold nanoparticles. The blue-shifting of the C–N stretching mode and its intensity enhancement is suggestive of predominantly S-bound coordination by analogy with the behavior of bulk-phase metal–thiocyanate complexes;⁴⁶ the other vibrational information is also valuable for deciphering the nature of the surface SCN^- coordination. The S-binding mode is fingerprinted on the positively charged gold surface from the bands at ~ 736 and $\sim 451\text{ cm}^{-1}$. Here, it is worth mentioning that the ν_{CS} mode is too weak to permit any definite conclusion to be drawn, and the frequency of δ_{NCS} is between those observed for S-bonded ($\sim 420\text{ cm}^{-1}$) and uncoordinated thiocyanate ($\sim 480\text{ cm}^{-1}$).⁴⁶ A possible explanation for the disparate behavior of δ_{NCS} is that it may arise from thiocyanate adsorbed at different sites and possibly in an orientation different from the adsorbate responsible for the observed stretching modes. It has been speculated that the SERS effect for a given vibrational mode requires a component of the polarization vector to lie normal to the surface.⁴⁸ Although this would be achieved for the ν_{CN} and ν_{CS} modes by the tilted

TABLE 4: Experimental and Calculated SERS Frequencies (in cm^{-1}) of Different Models of Au–NH₄SCN Interaction Using the B3LYP/Lan12DZ Level of Theory

positively charged Au colloid	model A	model B	model C	model D	model E	negatively charged Au colloid
	3515	3554	3562	3515	3518	
	3412	3427	3432	3412	3413	
	3078			3085	3015	
2114	2232	2270				
		2204	2195	2110	2181	2068
			1895			
	1786	1795	1789	1785	1788	
1631	1635	1663	1669	1634	1640	1660
1567	1573			1572	1566	
		1495	1459			
			711			750
645	621	685		645	635	
			532			
		520	519			
		502				
	462					
451	445	443	449	453	448	
			415	428		
		406				
	377			373	379	
312			314	353		
		291				
	255	272	262			
240	215			216		
					194	201
	177			179		
			159	158		
	117	122	121	116	126	
			95	92	101	
		90	87	89	93	
	60		61	61	66	
	35	49	33		50	
		19	23	23	27	
			11	12	12	

perpendicular configuration normally expected for adsorbed thiocyanate,⁴⁹ appearance of the δ_{NCS} mode may require a relatively flat orientation on the surface, so a more diagnostic

**Figure 15.** Simulated SERS spectrum of thiocyanate with CPC-stabilized (positively charged) gold colloid.

feature in this regard is the metal surface–adsorbate ($\nu_{\text{m-a}}$) band. Its emergence at $\sim 240 \text{ cm}^{-1}$ in the SERS spectra typically prescribes the formation of Au–S bond.⁵⁰ This bond formation probably results from electrostatic attraction between oppositely charged metal surface and probe, which is also accountable from “soft (S)–soft (Au)” interaction, as depicted by the SHAB (soft hard acid base) principle. Hence, in solution phase, CPC offers unique stabilization to the Au clusters on one hand and does not inhibit the diffusive interaction of SCN^- with the surface atom of Au on the other. Thus, SHAB theory favors actively despite its (CPC) chainlike structure. Now it is simple to interpret the movement of the C–N stretching mode to higher frequency value. Coordination of SCN^- through “S” restricts the delocalization of a negative charge on sulfur, with the π electrons of “C=N” corroborating the increase in the effective bond order and bond strength. Analyzing the SERS spectrum of thiocyanate for citrate-stabilized gold sol, we may conclude that in its case, SCN^- adsorption is predominantly physisorption, whereas it is chemisorbed in an end-on perpendicular fashion through sulfur on a CPC-stabilized gold surface.

To have a precise idea regarding the interaction of the SCN^- , we have estimated the apparent enhancement factors (AEFs) of a selected Raman band for both positively and negatively charged colloids using the following relation.⁵¹ Accordingly,

$$\text{AEF} = \sigma_{\text{SERS}}[C_{\text{NRS}}]/\sigma_{\text{NRS}}[C_{\text{NRS}}]$$

where C_{NRS} and C_{SERS} are the concentrations of SCN^- in aqueous solution and in positively/negatively charged colloids, respectively, and σ_{NRS} and σ_{SERS} represent the peak areas of the NRS and SERS bands measured from the baseline. They are shown in Table 3. The real enhancement factor will be a few orders of magnitude higher than that shown in Table 3 because (i) the number of molecules adsorbed on the positively and negatively charged colloidal surface is less than actually present in the colloid and (ii) the intensity of the laser excitation is significantly reduced in the gold sol as compared with that in solution owing to absorption and scattering by gold nanoparticles.

The result is clear evidence of chemical enhancement^{52a–d} in our case which engrosses a charge transfer (CT) mechanism. In a true sense, the chemical and electromagnetic mechanisms collectively contribute to SERS enhancement and are not readily separable.^{52e} Any theoretical approach that challenge separating them will probably fail in one or more limits. Thus, an electromagnetic factor can also share in the enhancement observed in our case due to the different environment factors.

4.2.2. Model Surface Complexes: A Treatment by DFT. To contemplate the origin of different bands in the SERS spectra, calculations of model surface complexes constituted by molecules bound to metal atoms have been performed to provide useful information about the interaction between the adsorbate and metal substrate. This introduction of simple computational models and their validation using archetypal chemisorbed analytes has been shown to be of great utility in understanding the interactions.⁵³

DFT calculations on five different model complexes (for thiocyanate and Au sol having positively charged surface) considering the interaction of adsorbate through its sulfur (S_6) end in all the models have been carried out, and these are shown in Figure 14. The first one having two positively charged gold atoms [hereafter Au(+)] bound to the sulfur atom (model A); the second one consisting of one Au(+) (model B); the other three comprising three gold atoms arranged in a triangular fashion: model C includes two Au(0) and one Au(+) through which the interaction takes place. In two other remaining models,

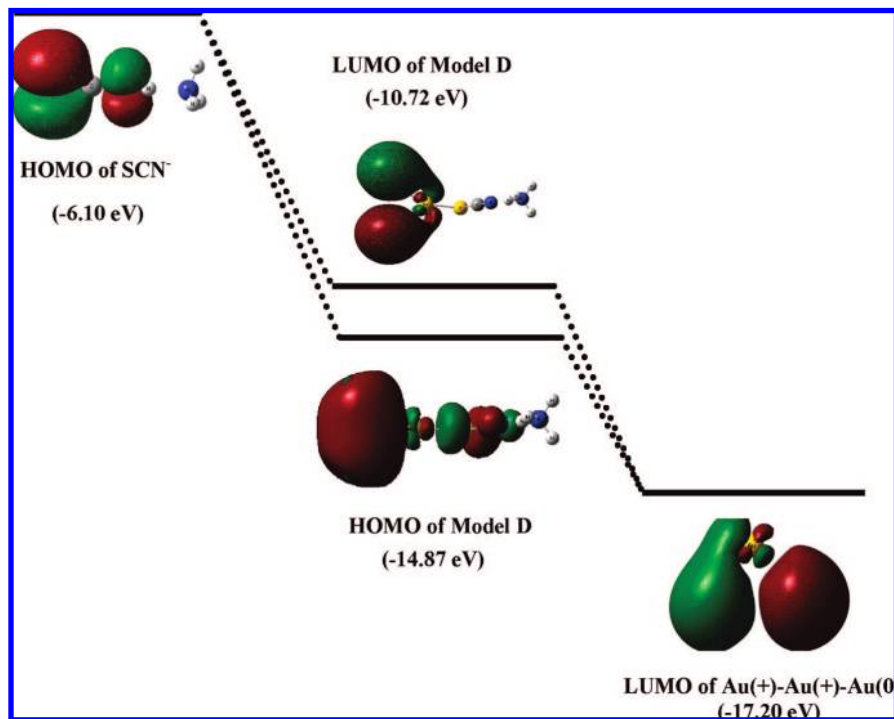


Figure 16. Frontier molecular orbital scheme of charge-transfer complex formation between NH_4SCN and triatomic gold clusters.

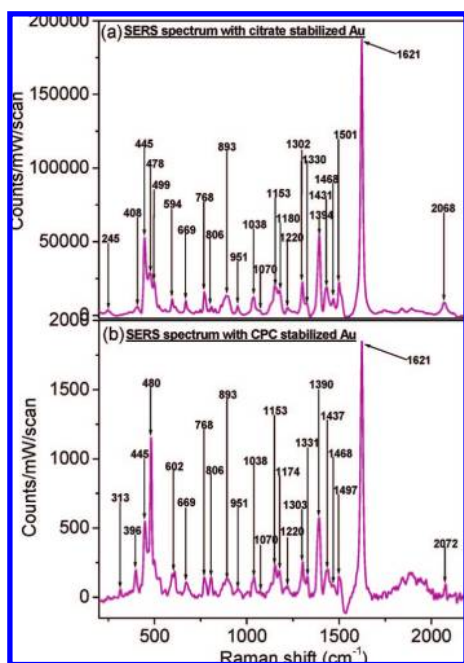


Figure 17. SERS spectra of MB^+ at concentration 10^{-5} M with (a) citrate- and (b) CPC-stabilized Au colloid.

we have two $\text{Au}(+)$ and one $\text{Au}(0)$ in the three apex of the triangle, but a difference in interaction appears in the sense that in model D, the $\text{Au}(+)$ in the apex is near the adsorptive site of the molecule, whereas in model E, the base of the triangle is near the adsorptive site; that is, S_6 . The foremost aim of these types of calculations is to identify the species really adsorbed on the gold surface by the best agreement with the SERS bands. Table 4 shows the calculated frequencies of five probable model complexes along with the experimentally observed SERS bands (selected) for the two kinds of gold colloidal solution. As one can see from this table and from Figure 15 (simulated spectra), theoretically predicted frequencies for the model D complex satisfactorily match the experimental results within a tolerable

TABLE 5: Observed SERS Bands (Up to 1800 cm^{-1}) of the Molecule (MB^+) on Positive and Negatively Charged Au Colloid, Apparent Enhancement Factor (AEF) (with Respect to 1621 cm^{-1} Band) and Their Tentative Assignments^a

positively charged Au colloid		negatively charged Au colloid		tentative assignments
SERS (cm^{-1})	AEF	SERS (cm^{-1})	AEF	
1621s	2×10^2	1621s	2×10^4	$\nu(\text{C}-\text{C})_{\text{ring}}$ $\nu(\text{C}-\text{N}-\text{C})_{\text{ring}}$
1497w		1501w		$\nu(\text{C}-\text{C})_{\text{ring}}$
1468vww		1468vw		$\nu(\text{C}-\text{C})_{\text{ring}}$
1437w		1431w		$\nu(\text{C}-\text{C})_{\text{ring}}$
1390m		1394m		$\nu(\text{CN})_{\text{sym}}$
1331vw		1330sh		$\nu(\text{CN})_{\text{asym}}$
1303w		1302w		$\nu(\text{C}-\text{C})_{\text{ring}}$
1220vw		1220vww		
1174sh		1180vww		
1153vw		1153vw		$\beta(\text{C}-\text{H})$
1070vww		1070sh		$\nu(\text{C}-\text{S}-\text{C})_{\text{asym}}$
1038w		1038w		$\beta(\text{C}-\text{H})$
951vw		951vw		
893w		893w		
806vww		806vww		
768sh		768w		
669w		669vw		$\gamma'(\text{C}-\text{H})$
602w		594vw		$\delta(\text{CCC})_{\text{in-plane}}$ skeletal deformation
		499vww		
480vw		478vww		$\delta(\text{CNC})$ skeletal deformation
445w		445w		$\delta(\text{CNC})$ skeletal deformation
396m		408vww		$\delta(\text{CSC})$ skeletal deformation
313w		245vww		$\nu(\text{Au}-\text{S})$

^a ν , stretching; β , in-plane bend; δ , skeletal deformation; sh, shoulder.

limit. Calculations of interaction energies for different models by means of basis set superposition error (BSSE) using the

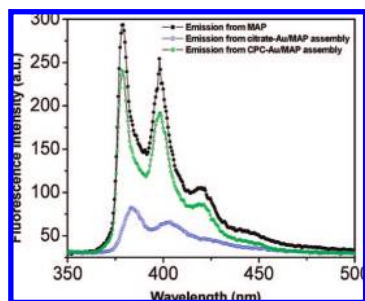


Figure 18. Emission spectra of MAP and the MAP–Au assembly.

counterpoise approach were observed to be more susceptible. The BSSE-corrected energy for the five models are shown in Figure 14. Moreover, model D was also found to be thermodynamically more stable from the isolated thiocyanate and three-atom-gold clusters. This stabilization is attributed to the Au–S binding energy. Again, Table 1 gives the perturbation in C₇–S₆ and C₇–N₈ bond lengths of thiocyanate before and after adsorption. The increase in the C–S bond length and the decrease in the C–N bond length give a clear confirmation about the bonding of thiocyanate through S₆ to the metal surface.

4.2.3. Charge Transfer (CT) between Thiocyanate and Gold Surface. This CT mechanism of SERS can be explained by the resonant Raman mechanism.^{54a} Several research groups have also implicated the adsorption-induced charge transfer mechanism to support the importance of a surface-related resonant electronic state in producing the enhancement. The electron–hole pair excitation hypothesis and atomic scale roughness factor, as brought into the picture by Otto and co-workers, may also play an important role in assisting this charge transfer enhancement mechanism.^{54b–g} Molecule-to-metal CT excitation occurs when an electron is transferred from the highest occupied molecular orbital (HOMO) of the adsorbate to the lowest unoccupied molecular orbital (LUMO) of the metal/metal cluster acceptor. Conversely, the transfer of an electron from the HOMO of the metal/metal cluster to the LUMO of adsorbate results in metal-to-molecule charge transfer transition. To examine the direction of the CT interaction in our case, the HOMO energy of NH₄SCN has been estimated from the DFT calculation. The theoretical results show that the HOMO energy of the molecule is ~ -6.10 eV, which is energetically higher than the LUMO energy (-17.20 eV) of the three-atom gold cluster (as in model D). Again, natural population analysis obtained from DFT calculations shows that the partial charge on S₆ before adsorption is $\sim -0.136 e$ and after adsorption (model D) is $\sim 0.459 e$. These theoretical findings collaboratively address the charge transfer (CT) phenomenon from a molecule-to-metal surface. According to frontier molecular orbital approach, the CT transition⁵⁵ is represented in Figure 16.

4.2.4. SERS Spectra of Methylene Blue. The thrust of our findings obtained so far for negatively charged thiocyanate was authenticated by examining the SERS spectrum of a cationic dye, methylene blue, with the same gold colloidal solutions (Figure 17). The 632.8 nm excitation radiation is coincident with an absorption maximum ($\lambda_{\text{max}} = 664$ nm) of MB⁺, enabling a resonance-enhancement process to play a major role in the generation of the Raman signal (SERRS) in this case. Table 5 lists the major bands, and the assignments in the table are based on the analyses of the SERS spectra of MB⁺ reported earlier.⁵⁶ The spectral pattern harmonized well with those reported spectra. Several striking changes in relative band intensities are observed for two types of gold sol. For citrate-capped gold, the bands

are more intense and the enhancement factor is observed to be $\sim 2 \times 10^4$ whereas for CPC-stabilized gold, the enhancement is $\sim 2 \times 10^2$ (with reference to the 1621 cm⁻¹ band) (Table 5). This result reflects our earlier conjecture in a sense that here, citrate-stabilized gold nanoparticles with a negative surface charge offer a favorable interactive circumference toward this cationic dye molecule rather than thiocyanate and are, thus, able to give better SERS enhancement.

4.3. Study of Fluorescence Quenching of 1-Methylaminopyrene. The ability of the gold surface to bind with specific functional groups has made it a suitable agent for optoelectronic applications such as fluorescence patterning.⁵⁷ Fluorescence spectroscopy can provide valuable information about the intermolecular interactions. It has already been spelled out that an electrostatic field force unequivocally supports the SERS results, whereas appropriately gold surface charges were considered for SCN⁻ and the cationic dye, MB⁺. For further support, we extended our study to observe the fluorescence effect. For this, we have brought in the 1-methylaminopyrene as the fluorescence probe to scrutinize the findings when it is assembled with gold nanoparticles in solution. Figure 18 shows the fluorescence spectra of MAP aqueous solution and when it is in two types of gold colloidal solution. An aqueous solution of MAP possesses well-defined emission bands ($\lambda_{\text{ex}} \sim 278$ nm) with maxima at 379, 398, and 420 nm, which can be attributed to the monomeric form of the fluorophore.⁵⁸ Damping of the surface plasmon band is observed after treatment with gold colloid that indicates the attachment of the probe molecule on the particle surface.⁵⁹ The outcome of such attachment was quenching of the MAP emission. This was more pronounced in the case of citrate-stabilized gold sol than in that of CPC-stabilized gold sol. The mechanism behind the quenching of the excited states of a fluorophore lies in the fact that when a donor molecule is placed in the vicinity of a conductive metal surface, a resonant energy transfer between the donor and acceptor takes place.⁶⁰ The sequential substitutions of stabilizer ions from the nanoparticle surface by the terminal amino group of the MAP, followed by interaction of the amino group with the vacant orbitals of these coordinatively unsaturated surface atoms, presumably happens due to dipole–dipole interaction; that is, through FRET (Forster resonance energy transfer) mechanism. This energy transfer process also has a dependency on the spectral overlap of the donor emission spectrum and the acceptor absorption spectrum⁵⁹ and on the distance between the donor and the acceptor. Thus, the free electron pair on the nitrogen of the MAP is arrested. So the emission is only from the unbound probe molecules in the system, as reported in earlier literature.⁶¹ On the electrostatic ground, CPC-stabilized gold nanoparticles are expected to be a better quencher than citrate-capped gold nanoparticles due to the favorable dipole–dipole interaction between the positively charged surface of the gold nanoparticles and the lone pair electron of MAP, but we experienced the reverse, which is explainable by the distance-dependent fluorescence quenching mechanism. Now it is worth mentioning that cetylpyridinium cations can provide a sterically more hindered environment around the gold nanoparticles as compared to that of citrate ions. The probe molecules thus remain far apart from the CPC-stabilized gold surface, and the substitution of citrate ions becomes more facile. Thus, for citrate ions, higher numbers of MAP molecules are engaged in the long-range energy transfer via through-bond electronic coupling⁶² with the metal surface, and a higher degree of quenching is observed. This is why the observed fluorescence phenomenon

could not provide a direct support to the observed SERS result because of the distance-dependent consequence.

5. Conclusion

In summary, a facile and environmentally friendly approach has been applied for the quantitative recovery of anion-exchange, resin-bound, citrate-stabilized gold nanoparticles using a cationic surfactant, cetylpyridinium chloride. Of special interest is the discrete behavioral nature of the two types of gold colloids and their proficiency as a SERS substrate. Most interestingly, cetylpyridinium-stabilized gold has been found to be the superior SERS substrate over negatively charged (citrate-stabilized) nanoparticles. The adsorption behavior has been investigated by SERS aided by density functional theory. The observed vibrational bands have been assigned from the potential energy distributions. Optimized structural parameters of the free and modeled adsorbed molecule have been estimated from the above-mentioned level of theory. Analyzing the results, we infer that thiocyanate is chemisorbed on a positively charged gold surface through the sulfur end in a perpendicular fashion, which is substantiated by (i) the appearance of a Au–S vibrational mode at $\sim 240\text{ cm}^{-1}$ and (ii) blue-shifting of the $\text{C}\equiv\text{N}$ stretching frequency (ν_{CN}); whereas, on a negatively charged gold surface, only physisorption occurs. This chemisorption leads to molecule-to-metal charge transfer, as pointed out by the enhancement factor calculation. A similarly negatively charged colloid acts comparably as a better sensor for MB^+ . Therefore, the specificity of vibrational spectroscopy in conjunction with DFT for monitoring metal–analyte interaction at their interface makes SERS an ideal tool for probing such interfaces. Thus in the not too distant future, one can imagine that SERS, coupled with increasingly sophisticated theory and experimental affirmation, will be a superior platform to measure chemical, physical, and biological phenomena on the submicrometer scale in real time.

Acknowledgment. This work is dedicated to Prof. J. A. Creighton for his pioneering work in surface enhanced Raman spectroscopy. The authors are thankful to the CSIR, UGC, NST, and DST, New Delhi, and Indian Institute of Technology, Kharagpur, for financial assistance.

References and Notes

- (1) Fleischman, M.; Hendra, P. J.; McQuillan, A. J. *Chem. Phys. Lett.* **1974**, *26*, 163.
- (2) (a) Jeanmaire, D. J.; Van Duyne, R. P. *J. Electroanal. Chem.* **1977**, *84*, 1. (b) Albrecht, M. G.; Creighton, J. A. *J. Am. Chem. Soc.* **1977**, *99*, 5215.
- (3) (a) Bukowska, J. J. *Mol. Struct.* **1992**, *275*, 151. (b) Chowdhury, J.; Ghosh, M.; Misra, T. N. *Spectrochim. Acta, Part A* **2000**, *56*, 2107.
- (4) (a) Pettinger, B.; Lipkowski, J.; Ross, P. N. *Adsorption at Electrode Surface* **1992**, 285. (b) Tian, Z. Q.; Ren, B. *Annu. Rev. Phys. Chem.* **2004**, *55*, 197.
- (5) (a) Nie, S.; Emory, S. R. *Science* **1997**, *275*, 1102. (b) Kneipp, K.; Wang, Y.; Kneipp, H.; Perelman, L. T.; Itzkan, I.; Dasari, R. R.; Feld, M. S. *Phys. Rev. Lett.* **1997**, *78*, 1667. (c) Goulet, P. J. G.; Aroca, R. F. *Anal. Chem.* **2007**, *79*, 2728.
- (6) (a) Ni, J.; Lipert, R. J.; Dawson, G. B.; Porter, M. D. *Anal. Chem.* **1999**, *71*, 4903. (b) Kim, N. H.; Lee, S. J.; Kim, K. *Chem. Commun.* **2003**, 724. (c) Cao, P.; Gu, R.; Tian, Z. Q. *Langmuir* **2002**, *18*, 7609. (d) Chu, W.; LeBlanc, R. J.; Williams, C. T.; Kubota, J.; Zaera, F. J. *Phys. Chem. B* **2003**, *107*, 14365. (e) Mettugh, C. J.; Keir, R.; Graham, D.; Smith, W. E. *Chem. Commun.* **2002**, 580. (f) Tian, Z. Q.; Ren, B.; Wu, D. Y. *J. Phys. Chem. B* **2002**, *106*, 9463.
- (7) (a) Sanchez-Gil, J. A.; Garcia-Ramos, J. V. *Chem. Phys. Lett.* **2003**, *367*, 361. (b) Sanchez-Gil, J. A.; Garcia-Ramos, J. V.; Mendez, E. R. *Phys. Rev. B* **2001**, *62*, 10515.
- (8) (a) Kneipp, K.; Kneipp, H.; Itzkan, I.; Dasari, R. R.; Feld, M. S. *Chem. Rev.* **1999**, *99*, 2957. (b) Sackmann, M.; Materny, A. *J. Raman Spectrosc.* **2006**, *37*, 305. (c) Campion, A.; Kambhampati, P. *Chem. Soc. Rev.* **1998**, *27*, 241. (d) Jensen, L.; Aikens, C. M.; Schatz, G. C. *Chem. Soc. Rev.* **2008**, *37*, 1061.
- (9) (a) Otto, A., In *Light Scattering in Solids*; Cardona, M., Guentherodt, G., Eds.; Springer: Berlin, 1984. (b) Moskovits, M. *Rev. Mod. Phys.* **1985**, *57*, 783. (c) Moskovits, M. *Top. Appl. Phys.* **2006**, *103*, 1. (d) Kneipp, K.; Kneipp, H. *Isr. J. Chem.* **2006**, *46*, 299.
- (10) (a) Musick, M. D.; Keating, C. D.; Lyon, L. A.; Botsko, S. L.; Pena, D. J.; Hollay, W. D.; McEvoy, T. M.; Richardson, J. N.; Natan, M. J. *Chem. Mater.* **2000**, *12*, 2869. (b) Park, S.-H.; Im, J.-H.; Im, J.-W.; Chun, B.-H.; Kim, J.-H. *Microchem. J.* **1999**, *63*, 71.
- (11) (a) Lacy, W. B.; Olson, L. G.; Harris, J. M. *Anal. Chem.* **1999**, *71*, 2564. (b) Mulvaney, S. P.; He, L.; Natan, M. J.; Keating, C. D. *J. Raman Spectrosc.* **2003**, *34*, 163. (c) Reilly, T. H.; Corbman, J. D.; Rowlen, K. L. *Anal. Chem.* **2007**, *79*, 5078.
- (12) (a) Li, J.; Fang, Y. *Spectrochim. Acta, Part A* **2007**, *66A*, 994. (b) Murgida, D.; Hildebrandt, P. *Top. Appl. Phys.* **2006**, *103*, 313.
- (13) Pristinski, D.; Tan, S.; Erol, M.; Du, H.; Sukhishvili, S. *J. Raman Spectrosc.* **2006**, *37*, 762.
- (14) (a) Orendorff, C. J.; Gearheart, L.; Jana, N. R.; Murphy, C. J. *Phys. Chem. Phys.* **2006**, *8*, 165. (b) Yang, Y.; Xiong, L.; Shi, J.; Nogami, M. *Nanotechnology* **2006**, *17*, 2670. (c) White, D. J.; Mazzolini, A. P.; Stoddart, P. R. *J. Raman Spectrosc.* **2007**, *38*, 377.
- (15) (a) Tian, Z.-Q.; Yang, Z.-L.; Ren, B.; Li, J.-F.; Zhang, Y.; Lin, X.-F.; Hu, J.-W.; Wu, D.-Y. *Faraday Discuss.* **2006**, *132*, 159. (b) McLellan, J. M.; Siekkinen, A.; Chen, J.; Xia, Y. *Chem. Phys. Lett.* **2006**, *427*, 122. (c) Kundu, S.; Maheshwari, V.; Niu, S.; Saraf, R. F. *Nanotechnology* **2008**, *19*, 065604. (d) Pande, S.; Jana, S.; Basu, S.; Sinha, A. K.; Datta, A.; Pal, T. *J. Phys. Chem. C* **2008**, *112*, 3619.
- (16) Lu, L.; Kobayashi, A.; Tawa, K.; Ozaki, Y. *Chem. Mater.* **2006**, *18*, 4894.
- (17) (a) Lee, P. C.; Meisel, D. *J. Phys. Chem.* **1982**, *86*, 3391. (b) Boesch, S. E.; York, S. S.; Frech, R.; Wheeler, R. A. *Phys. Chem. Comm.* **2001**, *4*, 1. (c) Nickel, U.; Mansyreff, K.; Schneider, S. *J. Raman Spectrosc.* **2004**, *35*, 101. (d) Leopold, N.; Lendl, B. *J. Phys. Chem. B* **2003**, *107*, 5723.
- (18) (a) Yea, K. H.; Lee, S.; Kyong, J. B.; Choo, J.; Lee, E. K.; Joo, S. W.; Lee, S. *Analyst* **2005**, *130*, 1009. (b) Wang, W.; Ruan, C.; Gu, B. *Anal. Chim. Acta* **2006**, *567*, 121. (c) Ruan, C.; Wang, W.; Gu, B. *Anal. Chim. Acta* **2006**, *567*, 114. (d) Mosier-Boss, P. A.; Lieberman, S. H. *Appl. Spectrosc.* **2003**, *57*, 1129. (e) Mosier-Boss, P. A.; Lieberman, S. H. *Appl. Spectrosc.* **2000**, *54*, 1126.
- (19) (a) Tan, S.; Erol, M.; Attygalle, A.; Du, H.; Sukhishvili, S. *Langmuir* **2007**, *23*, 9836. (b) Tan, S.; Erol, M.; Sukhishvili, S.; Du, H. *Langmuir* **2008**, *24*, 4765.
- (20) (a) Schlesinger, M.; Paunovic, M. *Modern Electroplating*, 4th ed.; John Wiley & Sons: New York, 2000. (b) Bachelon, P.; Corset, J.; De Loze, C. *J. Solution Chem.* **1980**, *9*, 129. (c) Pande, S.; Ghosh, S. K.; Nath, S.; Praharaj, S.; Jana, S.; Panigrahi, S.; Basu, S.; Pal, T. *J. Colloid Interface Sci.* **2006**, *299*, 421.
- (21) (a) Schwerdtfeger, P.; Boyd, P. D. W.; Burrell, A. K.; Robinson, W. T.; Taylor, M. J. *Inorg. Chem.* **1990**, *29*, 3593. (b) Panattoni, C.; Frasson, E. *Acta Crystallogr.* **1963**, *16*, 1258. (c) Gronbaek, R.; Dunitz, J. D. *Helv. Chim. Acta* **1964**, *47*, 1889.
- (22) (a) Luo, H.; Weaver, M. J. *Langmuir* **1999**, *15*, 8743. (b) Corrigan, D. S.; Gao, P.; Leung, L.-W. H.; Weaver, M. J. *Langmuir* **1986**, *2*, 744. (c) Zou, S.; Weaver, M. J.; Li, X. Q.; Ren, B.; Tian, Z.-Q. *J. Phys. Chem. B* **1999**, *103*, 4218. (d) Gao, P.; Weaver, M. J. *J. Phys. Chem.* **1986**, *90*, 4057. (e) Tian, Z.-Q.; Lin, W. F.; Mao, B. W. *J. Electroanal. Chem.* **1991**, *319*, 403. (f) Lin, X.-F.; Ren, B.; Yang, Z.-L.; Liu, G.-K.; Tian, Z.-Q. *J. Raman Spectrosc.* **2005**, *36*, 606.
- (23) (a) Tang, W.; Xu, H.; Kopelman, R.; Philbert, M. A. *Photochem. Photobiol.* **2005**, *81*, 242. (b) Zeiler, T.; Riess, H.; Wittmann, G.; Hintz, G.; Zimmerman, R.; Muller, C.; Heuft, H. G.; Huhn, D. *Transfusion* **1994**, *34*, 685. (c) Orth, K.; Ruck, A.; Stanescu, A.; Beger, H. G. *Lancet* **1995**, *345*, 519. (d) Gurr, E. *Staining—Practical and Theoretical*, 2nd ed.; Williams and Watkins: Baltimore, MD, 1962; p 303. (e) Halliwell, B.; Gutteridge, J. M. C. In *Free Radicals in Biology and Medicine*; Oxford University Press: New York, 1989. (f) Johnson, B. E.; Ferguson, J. *Semin. Dermatol.* **1990**, *9*, 39.
- (24) Atherton, S. J.; Harriman, A. *J. Am. Chem. Soc.* **1993**, *115*, 1816.
- (25) (a) Szezhalmi, A. V.; Erdmann, M.; Engel, V.; Schmitt, M.; Amthor, S.; Kriegisch, V.; Noll, G.; Stahl, R.; Lambert, C.; Leusser, D.; Stalke, D.; Zabel, M.; Popp, J. *J. Am. Chem. Soc.* **2004**, *126*, 7834. (b) Johansson, P. *Phys. Chem. Chem. Phys.* **2005**, *7*, 475.
- (26) (a) Scott, A. P.; Radom, L. *J. Phys. Chem.* **1996**, *100*, 16502. (b) Wong, M. W. *Chem. Phys. Lett.* **1996**, *256*, 391.
- (27) (a) Halls, M. D.; Schlegel, H. B. *J. Chem. Phys.* **1998**, *109*, 10587. (b) Halls, M. D.; Schlegel, H. B. *J. Chem. Phys.* **1999**, *111*, 8819.
- (28) (a) Li, X.; Gewirth, A. *J. Am. Chem. Soc.* **2003**, *125*, 11674. (b) Tielens, F.; Saeys, M.; Tourwé, E.; Marin, G. B.; Hubin, A.; Geerlings, P. *J. Phys. Chem. A* **2002**, *106*, 1450.
- (29) Frens, G. *Nat. Phys. Sci.* **1973**, *241*, 20.
- (30) Frisch, M. J.; Trucks, G. W.; Schlegel, H. B.; Scuseria, G. E.; Robb, M. A.; Cheeseman, J. R.; Montgomery, J. A.; Vreven, T., Jr.; Kudin, K. N.;

- Burant, J. C.; Millam, J. M.; Iyengar, S. S.; Tomasi, J.; Barone, V.; Mennucci, B.; Cossi, M.; Scalmani, G.; Rega, N.; Petersson, G. A.; Nakatsuji, H.; Hada, M.; Ehara, M.; Toyota, K.; Fukuda, R.; Hasegawa, J.; Ishida, M.; Nakajima, T.; Honda, Y.; Kitao, O.; Nakai, H.; Klene, M.; Li, X.; Knox, J. E.; Hratchian, H. P.; Cross, J. B.; Adamo, C.; Jaramillo, J.; Gomperts, R.; Stratmann, R. E.; Yazyev, O.; Austin, A. J.; Cammi, R.; Pomelli, C.; Ochterski, J. W.; Ayala, P. Y.; Morokuma, K.; Voth, G. A.; Salvador, P. J.; Dannenberg, J.; Zakrzewski, V. G.; Dapprich, S.; Daniels, A. D.; Strain, M. C.; Farkas, O.; Malick, D. K.; Rabuck, A. D.; Rahgavachari, K.; Foresman, J. B.; Ortiz, J. V.; Cui, Q.; Baboul, A. G.; Clifford, S.; Cioslowski, J.; Stefanov, B. B.; Liu, G.; Liashenko, A.; Piskorz, P.; Komaromi, I.; Martin, R. L.; Fox, D. J.; Keith, T.; Al-Laham, M. A.; Peng, C. Y.; Nanayakkara, A.; Challacombe, M.; Gill, P. M. W.; Johnson, B.; Chen, W.; Wong, M. W.; Gonzalez, C.; Pople, J. A. *Gaussian 03*, Gaussian, Inc.: Pittsburgh, PA, 2003.
- (31) Becke, A. D. *J. Chem. Phys.* **1993**, *98*, 5648.
- (32) Lee, C.; Yang, W.; Parr, R. G. *Phys. Rev. B* **1988**, *37*, 785.
- (33) (a) Frisch, M. J.; Pople, J. A.; Binkley, J. S. *J. Chem. Phys.* **1984**, *80*, 3265. (b) Cardini, G.; Muniz-Miranda, M. *J. Phys. Chem. B* **2002**, *106*, 6875. (c) Vivoni, A.; Birke, R. L.; Foucault, R.; Lombardi, J. R. *J. Phys. Chem. B* **2003**, *107*, 5547.
- (34) Martin, J. M. L.; Alsenoy, C. V. *GAR2PED*, University of Antwerp: Antwerp, Belgium, 1995.
- (35) (a) Sarkar, J.; Chowdhury, J.; Ghosh, M.; De, R.; Talapatra, G. B. *J. Phys. Chem. B* **2005**, *109*, 12861. (b) Sarkar, J.; Chowdhury, J.; Ghosh, M.; De, R.; Talapatra, G. B. *J. Phys. Chem. B* **2005**, *109*, 22536.
- (36) Aroca, R. F.; Clavijo, R. E.; Halls, M. D.; Schlegel, H. B. *J. Phys. Chem. A* **2000**, *104*, 9500.
- (37) (a) Bolboaca, M.; Iliescu, T.; Paizs, Cs.; Irimie, F. D.; Kiefer, W. *J. Phys. Chem. A* **2003**, *107*, 1811. (b) Giese, B.; McNaughton, D. *J. Phys. Chem. B* **2002**, *106*, 101. (c) Pergolese, B.; Bigotto, A. *J. Raman Spectrosc.* **2002**, *33*, 646. (d) Mukherjee, K.; Sanchez-Cortes, S.; Garcia-Ramos, J. V. *Vibr. Spectrosc.* **2001**, *25*, 91.
- (38) (a) Kerker, M. *The scattering of light and other electromagnetic radiation*; Academic: New York, 1969. (b) Ordal, M. A.; Long, L. L.; Bell, R. J.; Bell, S. E.; Bell, R. R.; Alexander, J. R. W.; Ward, C. A. *Appl. Opt.* **1983**, *22*, 1099. (c) Ordal, M. A.; Bell, R. J.; Alexander, J. R. W.; Long, L. L.; Querry, M. R. *Appl. Opt.* **1985**, *24*, 4493. (d) Segelstein, D. J. *The complex refractive index of water*. Ph.D. Thesis, University of Missouri—Kansas City, Kansas City, MO, 1981.
- (39) Mayya, K. S.; Sastry, M. *Langmuir* **1998**, *14*, 6344.
- (40) (a) Praharaj, S.; Nath, S.; Ghosh, S. K.; Kundu, S.; Pal, T. *Langmuir* **2004**, *20*, 9889.
- (41) Kreisig, S. M.; Tarazona, A.; Koglin, E.; Schwuger, M. J. *Langmuir* **1996**, *12*, 5279.
- (42) Maye, M. M.; Zheng, W.; Leibowitz, F. L.; Ly, N. K.; Zhong, C.-J. *Langmuir* **2000**, *16*, 490.
- (43) (a) Liu, H.; Mao, G.; Meng, S. *J. Mol. Catal.* **1992**, *74*, 275. (b) Yu, W.; Wang, Y.; Liu, H.; Zheng, W. *J. Mol. Catal. A: Chem.* **1996**, *112*, 105. (c) Bönemann, H.; Brioux, W.; Brinkmann, R.; Fretzen, R.; Jousen, T.; Köppler, R.; Korall, B.; Neiteler, P.; Richter, J. *J. Mol. Catal.* **1994**, *86*, 129.
- (44) (a) Leff, D. V.; Ohara, P. C.; Heath, J. R.; Gelbart, W. M. *J. Phys. Chem.* **1995**, *99*, 7036. (b) Zhu, J.; Kónya, Z.; Puentes, V. F.; Kiricsi, I.; Miao, C. X.; Ager, J. W.; Alivisatos, A. P.; Somorjai, G. A. *Langmuir* **2003**, *19*, 4396.
- (45) Cullity, B. D.; Stock, S. R. *Elements of X-Ray Diffraction*, 3rd ed.; Prentice-Hall: Upper Saddle River, NJ, 2001; pp. 402.
- (46) Bailey, R. A.; Kozak, S. L.; Michelson, T. W.; Mills, W. N. *Coord. Chem. Rev.* **1971**, *6*, 407.
- (47) (a) Corrigan, D. S.; Foley, J. K.; Gao, P.; Pons, S.; Weaver, M. J. *Langmuir* **1985**, *1*, 616. (b) Weaver, M. J.; Barz, F.; Gordon, J. G., II.; Philpott, M. R. *Surf. Sci.* **1983**, *125*, 409.
- (48) (a) Allen, C. S.; Van Duyne, R. P. *Chem. Phys. Lett.* **1979**, *63*, 455. (b) Schatz, G. C.; Van Duyne, R. P. *Surf. Sci.* **1980**, *101*, 425.
- (49) Barcaly, D. J.; Caja, J. *Croat. Chem. Acta* **1971**, *43*, 221.
- (50) (a) Bourg, M.-C.; Badia, A.; Lennox, R. B. *J. Phys. Chem. B* **2000**, *104*, 6562. (b) Andreoni, W.; Curioni, A.; Grönbeck, H. *Int. J. Quantum Chem.* **2000**, *80*, 598.
- (51) (a) Chowdhury, J.; Ghosh, M.; Misra, T. N. *J. Colloid Interface Sci.* **2000**, *228*, 372. (b) Chowdhury, J.; Sarkar, J.; Tanaka, T.; Talapatra, G. B. *J. Phys. Chem. C* **2008**, *112*, 227. (c) Orendorff, C. J.; Gole, A.; Sau, T. K.; Murphy, C. J. *Anal. Chem.* **2005**, *77*, 3261.
- (52) (a) Zhao, L. L.; Jensen, L.; Schatz, G. C. *Nano Lett.* **2006**, *6*, 1229. (b) Lecomte, S.; Matejka, P.; Baron, M. H. *Langmuir* **1998**, *14*, 4373. (c) Campion, A.; Ivanecky, J. E., III.; Child, C. M.; Foster, M. J. *Am. Chem. Soc.* **1995**, *117*, 11807. (d) Doering, W. E.; Nie, S. *J. Phys. Chem. B* **2002**, *106*, 311. (e) Schatz, G. C. *Acc. Chem. Res.* **1984**, *17*, 370.
- (53) (a) Zhao, L. L.; Jensen, L.; Schatz, G. C. *J. Am. Chem. Soc.* **2006**, *128*, 2911. (b) Du, Y.; Fang, Y. *Spectrochim. Acta, Part A* **2004**, *60*, 535. (c) Cardini, G.; Muniz-Miranda, M.; Schettino, V. *J. Phys. Chem. B* **2004**, *108*, 17007. (d) Pergolese, B.; Muniz-Miranda, M.; Bigotto, A. *J. Phys. Chem. B* **2004**, *108*, 5698. (e) Sarkar, J.; Chowdhury, J.; Talapatra, G. B. *J. Phys. Chem. C* **2007**, *111*, 10049.
- (54) (a) Arenas, J. F.; Soto, J.; Lopez-Tocon, I.; Fernandez, D. J.; Otero, J. C.; Marcos, J. I. *J. Chem. Phys.* **2002**, *116*, 7207. (b) Pandey, P. K. K.; Schatz, G. C. *J. Chem. Phys.* **1984**, *80*, 2959. (c) Adrian, F. J. *Chem. Phys.* **1982**, *77*, 5302. (d) Gersten, J. I.; Birke, R. L.; Lombardi, J. R. *Phys. Rev. Lett.* **1979**, *43*, 147. (e) Otto, A. In *Light Scattering in Solids*; Cardona, M., Guntherodt, G., Eds.; Springer: West Berlin, Vol. 4. (f) Furtak, T. E. In *Advances in Laser Spectroscopy*; Garet, B. A., Lombardi, J. R., Eds.; Wiley: New York, 1983, vol. 2, p 175. (g) Persson, B. N. J. *Chem. Phys. Lett.* **1981**, *82*, 561.
- (55) (a) Hu, G.; Feng, Z.; Han, D.; Li, J.; Jia, G.; Shi, J.; Li, C. *J. Phys. Chem. C* **2007**, *111*, 8632. (b) Hu, G.; Feng, Z.; Li, J.; Jia, G.; Han, D.; Liu, Z.; Li, C. *J. Phys. Chem. C* **2007**, *111*, 11267.
- (56) (a) Xiao, G.-N.; Man, S.-Q. *Chem. Phys. Lett.* **2007**, *447*, 305. (b) Tognalli, N. G.; Feinstein, A.; Vericat, C.; Vela, M. E.; Salvarezza, R. C. *J. Phys. Chem. B* **2006**, *110*, 354. (c) Qin, L.; Zou, S.; Xue, C.; Atkinson, A.; Schatz, G. C.; Mirkin, C. A. *Proc. Natl. Acad. Sci. U.S.A.* **2006**, *103*, 13300. (d) Nicolai, S. H. A.; Rubim, J. C. *Langmuir* **2003**, *19*, 4291. (e) Naujok, R. R.; Duevel, R. V.; Corn, R. M. *Langmuir* **1993**, *9*, 1771.
- (57) Xu, P.; Yanagi, H. *Chem. Mater.* **1999**, *11*, 2626.
- (58) Thomas, K. G.; Kamat, P. V. *J. Am. Chem. Soc.* **2000**, *122*, 2655.
- (59) Ghosh, S. K.; Pal, A.; Kundu, S.; Nath, S.; Pal, T. *Chem. Phys. Lett.* **2004**, *395*, 366.
- (60) (a) Makarova, O. V.; Ostafin, A. E., Jr.; Norris, J. R.; Miesel, D. *J. Phys. Chem. B* **1999**, *103*, 9080. (b) Fan, C.; Wang, S.; Hong, J. W.; Bazan, G. C.; Plaxco, K. W.; Heeger, A. J. *Appl. Phys. Sci.* **2003**, *100*, 6297.
- (61) (a) Brust, M.; Walker, M.; Bethell, D.; Schiffrin, D. J.; Whyman, R. *J. Chem. Soc., Chem. Commun.* **1994**, 801. (b) Weitz, D. A.; Lin, M. Y. *Surf. Sci.* **1985**, *158*, 147. (c) Giersig, M.; Mulvaney, P. *Langmuir* **1993**, *9*, 3408.
- (62) Kittredge, K. W.; Fox, M. A.; Whitesell, J. K. *J. Phys. Chem. B* **2001**, *105*, 10594.

JP804028W